Rhinitis Radiofrequency Ablation: FEM analysis and experiments

by

Yuqi Song

B.S., Jilin University, 2014
M.S., Kansas State University, 2016

A THESIS

submitted in partial fulfillment of the requirements for the degree

MASTER OF SCIENCE

Department of Electrical and Computer Engineering
College of Engineering

KANSAS STATE UNIVERSITY
Manhattan, Kansas

2018

Approved by:

Major Professor
Dr. Punit Prakash

Copyright

Abstract

The primary objective of this research is to implement an experimentally validated computational model to guide device design and selection of energy delivery strategies for treating chronic rhinitis by radiofrequency ablation. Chronic rhinitis is one of the most common global health problems. It is not life-threatening but has a severe impact on quality of life. Direct cost by chronic rhinitis is enormous and places a burden on societies. Radiofrequency ablation is proposed to be as an efficient treatment providing symptom relief and avoiding side effects compared to traditional therapies. Three-dimensional finite element method (FEM) models were developed to investigate RFA devices and energy delivery strategies. FEM computational models could provide vital variable profiles that are technically challenging to determine through experiments. Also, computer simulation could reduce the number of experimental procedures during the device design process. First, single pair bipolar RF ablation experiments were performed to validate FEM simulations using the same geometry as in experiments. The data from experiments and simulations had a high correlation (R = 0.91). Second, the Neurent basket electrode was employed in experimental ablations in egg white, for comparison against FEM simulations. Smaller lesion sizes were observed in experiments compared to simulations, attributed to thermal convection that was not accounted for in simulation. Finally, FEM simulations were used to investigate the effects of basket electrode diameter, length, and applied power on ablation zone formation. A shorter but wider electrode with a maximum spacing distance between two pairs of electrodes is preferable to create discontiguous ablation zones. 50% duty cycle was recommended to create thermal ablation zones with gradually increasing temperature and sufficiently large thermal lesion volumes.

Table of Contents

List of Figures

List of Tables

Chapter 1 - Chronic Rhinitis

Rhinitis is a general term for inflammation of the mucous tissue of the nose [1]. The symptoms of rhinitis are rhinorrhea (commonly known as "running nose"), congestion, nasal itch, sneezing and postnasal drainage. Some patients may have an ocular problem such as watering eyes. Furthermore, rhinitis could aggravate other ear, nose and throat (ENT) conditions such as sinusitis, asthma, and otitis [2]. While not life-threatening, rhinitis may have a severe impact on an individual's quality of life.

Rhinitis can be either acute or chronic, chronic rhinitis is the focus of this research. There are three types of chronic rhinitis: allergic rhinitis, non-allergic rhinitis or mixed rhinitis which is a combination of allergic and non-allergic rhinitis [3]. Allergic rhinitis is an immune system disorder problem and is the most common cause of rhinitis. The immune system treats a typically harmless substance, known as allergens [4], as an intruder, and releases histamines and chemical mediators to respond to a false alarm. Pollen, dust mites, pet dander and mold spores are examples of common allergens. Allergic rhinitis may be seasonal or perennial. Seasonal allergic rhinitis is caused by sensitization to certain pollen or spores that are present during specific times of the year[3]. Perennial allergic rhinitis is caused by indoor allergens (such as dust and animal dander) and could occur any time of the year. The symptoms of allergic rhinitis include a runny nose, nasal itching and congestion and sneezing. Non-allergic rhinitis may occur for weeks to months at a time for up to a year. It may not have the other allergic manifestations such as itchy and runny noses, and also more persistent and less seasonal [5].

The most common treatment for allergic rhinitis is avoiding allergens which may be impractical and restrict an individual's daily life. Various medications have been developed to

relieve symptoms of allergic and non-allergic rhinitis, such as corticosteroids, antihistamines, decongestants, and anticholinergics [6]. These are typically delivered via nasal sprays and may have complications, such as nasal dryness, nosebleeds, headaches and throat dryness [7], while reducing rhinitis symptoms. Further, these medications usually require frequent administration once- or twice- daily for a relatively long period of time, thus impacting the quality of life of patients [6].

The impact of chronic rhinitis

Chronic rhinitis is one of the most common global health problems with seriously increasing incidence over the last decades [8]. Over 600 million people suffer from allergic rhinitis around the world which makes allergic rhinitis currently the most prevalent allergic disorder, affecting up to 30% of adults and 40% of children [9]. Although the prevalence of non-allergic rhinitis has not been studied definitively, it appears to be very common with an estimated prevalence in the United States of approximately 19 million [8]. Direct medical cost was $6.1 billion in 2000 and $11.2 billion in 2006 only in the US. This cost is much greater than other chronic diseases such as diabetes, coronary heart disease, and asthma [10] . The health and economic impact of rhinitis is grossly underestimated because most patients do not perceive the symptoms of rhinitis as a disease even though it has a huge influence on their social life, school and work [11]. Indirect losses due to rhinitis can place an additional burden on societies. In a word, the cost of either allergic or non-allergic chronic rhinitis is enormous. A more effective treatment for rhinitis needs to be developed to provide symptom relief and avoid the side effects of pharmacotherapy.

Radiofrequency ablation

Here, we investigate a minimally invasive treatment for chronic rhinitis, using radiofrequency ablation (RFA) for targeted destruction of offending nerves.

Radiofrequency (RF), in the medical field, includes the electromagnetic spectrum with frequency from 10 kHz to 800 kHz and almost always to a frequency close to 500 kHz. RFA is a minimally invasive interventional technique that has been performed in many medical fields, such as the elimination of cardiac arrhythmias, the destruction of tumors in different locations (liver, kidney, lung, bone, prostate, and breast) [12], or relief from chronic pain (back, neck, and arthritic joints) [13].

The principle of the basic RFA technique was presented by D'Arsonval in 1891, he demonstrated that when RF current passed through tissue, it caused an increase in tissue temperature [14]. The application of RFA in medical fields grew after the Bovie electrosurgical instrument was introduced by Cushing and Bovie in 1928 [15]. They used a continuous current to cut through tissue without inducing muscular contraction which had been a significant obstacle in neurosurgery. This revolutionary device enabled surgical procedures on patients with a brain mass that had previously been declared inoperable [16]. McGahan and colleagues applied selective RF electrodes on fresh liver superficially and deeply with ultrasound guidance in 1990. They replaced the traditional Bovie blade with specially designed needles with exposed distal tip [17]. They placed the needle deep into the liver to create hepatic lesions up to 10 mm in diameter. However, it was later shown by Goldberg that lesions with mean diameters larger than 16 mm could not be produced using a single probe due to charring the formation of electrically insulated charred tissue

[18]. In 1993, McGahan applied this new technique in human for surgeries treating liver tumors [19]. RFA needles were custom designed to achieve different surgical objectives. A monopolar needle with separate prongs deployable from the needle tip was designed by LeVeen in 1997 [20]. Goldberg investigated a creative approach to RF electrodes which enabled needle tip perfusion with chilled saline. Saline cools the tip of the electrodes, thereby delaying or preventing the formation of charred tissue, and thus facilitates creation of a larger region of coagulation. The cooling of electrodes tip will decrease temperature around the tip and help preventing charring formed around the electrodes [21]. Contemporary RF ablation studies have shown that generator power, local tissue characteristics and tissue interaction with RF current are important parameters in creating coagulation zones. Over the past years, more powerful generators (power range: 1 – 200 W) have been utilized and different electrode geometries have been designed based on specific requirements for varying clinical indications.

RFA is a relatively new method for treating nasal disease, and has been applied for the treatment of snoring, tonsillar hypertrophy, and non-allergic or allergic rhinitis. Most nasal RF generators employ bipolar electrodes with frequency from 100 to 4000 kHz. RFA creates an elliptical submucosal lesion in soft tissue, cause fibrosis of the underlying stroma leaving the surface epithelium intact, which makes nasal RFA different conventional RFAs in other sites [22]. Kezirian investigated the incidence of complications after temperature-controlled radiofrequency treatment of the inferior turbinates, palate, and tongue was low, and there were no complications of greater severity [23]. Patients may choose RFA as an efficient way of treating nasal problems with a low risk of complications. Celiker *et al* compared the efficacy of RF surgery to nasal steroid in 84 cases. In their study, measurement and patient questionnaire responses showed a clear

improvement by RF surgery in several symptoms, such as sneezing and headache, and a clinically significant improvement in nasal congestion and snoring [24].

RFA requires a radiofrequency generator, one or more active electrodes, and a return electrode (also, referred to as ground electrode). Active electrodes are placed within the target zone and the RF generator applies RF electrical current (450 ~ 500 kHz) to the tissue through the electrodes. The figure below shows a general setup of RF ablation, in this case illustrating a bipolar ablation. The current passes through target tissue and produces controlled heating on the target zone. The RF electrode is typically made of metal or alloy such as stainless steel, platinum, or Ni-Ti alloys are often used [25].

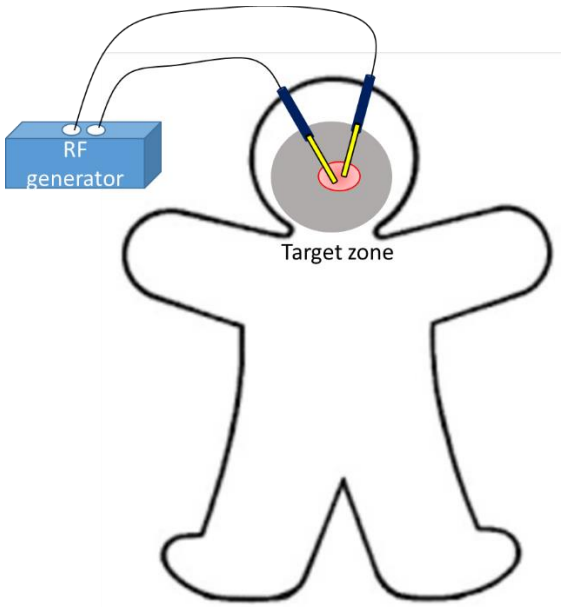

Figure 1-1 Illustration of RF generator and bipolar electrodes coupled to the patient

High-frequency alternating currents cause rapid oscillations of electrically-charged particles (ions) within the tissue. Rapid ion movement leads to frictional forces that induce thermal energy production and cause an elevation of tissue temperature, a process known as resistive

heating. Local increase in tissue temperature leads to the conduction of thermal energy to the adjacent tissue, resulting in the elevation of tissue temperature [26]. At elevated temperatures, tissue protein denaturation occurs, leading to cell death. Cell death due to heating depends on both time and temperature. As a rough guide line, it may take a few minutes to kill cells at 50 °C, but only a few seconds when temperature is above 60 °C

The highest tissue temperature during RF ablation ranges between 100 to 110 °C, and occurs in proximity to the active electrodes. Higher temperatures are typically not attained due to tissue vaporization and charring, both of which are electrically insulating. When tissue vaporization happens, a large portion of energy that contributes to temperature increase is used to change the water content of tissue into water gas [27]. Furthermore, tissue starts charring and forms carbonized tissue. The impedance of carbonized tissue is relatively high compared to normal tissue. The tissue charring is an irreversible process and prevents any further RF energy deposition [25]. Finally, tissue vaporization and charring will block coagulation zone growth around the target zone. Therefore, tissue temperature needs to be kept within desired range by controlling applied power during RF ablation procedure.

RFA is most commonly delivered with electrodes arranged in monopolar or bipolar configurations. Monopolar employs an active electrode with a small surface area that is placed within the target zone and a larger dispersive electrode (ground) to close the electrical circuit which is not intended to induce tissue heating and may be positioned on large muscle groups away from the target site, such as the patient's thigh [28]. Bipolar RFA uses two active electrodes with small surface areas, both positioned within the target zone [12]. Bipolar electrodes offer a more concentrated energy to a very specific area of tissue. With bipolar technique, the current is more tightly confined to the target zone and no return pad is required. Bipolar ablation will largely

decrease the risk of patient's skin burn under the ground pad, which is a noted complication of high power, long duration monopolar RFA. Multipolar RFA is performed by several pairs of bipolar electrodes, and actively switching between which pair is operating at a given time. These electrodes may have different dimensions, working times, and working powers [29].

In order to better understand the biophysical process during RFA, and also to investigate and develop optimized device geometries and energy delivery techniques for specific applications, computational models of RFA have been developed and widely used prior to experimental studies. Computational models are powerful tools for providing vital information on the electrical and thermal behavior of ablation, and are often less resource intensive than experimental approaches. The steps in building and using of a theoretical model are:

(1) Observation and simplification of the physical situation.

(2) Specification of the mathematical equations which govern the thermal and electrical phenomena.

(3) Specification of the boundary conditions, both electrical and thermal.

(4) Obtaining the physical characteristics (thermal and electrical) of the biological tissues and other materials included in the model.

(5) Choosing a numerical method in order to computationally or analytically achieve a solution.

(6) Conducting the post-processing of the computer results [12].

Objective

The primary objective of this research is to implement an experimentally validated computational model to guide device design and selection of energy delivery strategies for treating

chronic rhinitis by radiofrequency ablation. The system designed with this approach may be used for thermal destruction of engorged nasal mucosa and hypertrophied turbinates for chronic nasal disease in humans. This research will characterize the size and shape of damaged tissue zones following RF ablation with a novel basket electrode and generator by computer simulations and *in vivo* experiments.

Thesis outline

The rest of the thesis is organized as follows. Chapter 2 introduces background and review of techniques for RF ablation computer modeling. Chapter 3 describes experimental validation of the RF ablation computational models with a comparison between single bipolar RF ablation experiments and the corresponding FEM simulation. Chapter 4 compares the results from experiments with the Neurent basket electrode in egg white and simplified FEM simulation on tissue lesion size. It also investigates the effects of electrode geometry on ablation zone formation during the procedure and predicts tissue lesion formation with Nuerent basket electrode by computational simulations. Chapter 5 concludes the entire work and provides recommendation for further research efforts.

Chapter 2 - Radiofrequency Ablation Modeling

Computer modeling is a powerful tool to analyze RFA procedures, with applications to device design and optimization, comparative assessment of energy delivery strategies, and patient specific planning of ablation procedures. The main objective of computer-aided simulation with RFA is to allow for the prediction of thermal damage profiles caused by tissue heating during the ablation procedure. Computational models enable the characterization of spatial profiles of variables such as voltage and temperature during ablation. These values may be technically challenging to measure experimentally due to the need for use of invasive sensors. Besides, computer simulation further offers the potential to reduce the number of experimental procedures required to evaluate candidate device designs, thereby decreasing cost during the development cycle. Models are particularly useful for evaluating the impact of parameters such as electrode geometry, material properties, ablation duration, input power, frequency, and ablation device position on treatment outcome. The models are also excellent didactic tools that enable the users of RFA systems to become familiar with the equipment and procedures, and thus indirectly enhance the safety and efficacy of the therapies. [12] Therefore, the theoretical model not only supports the design and understanding of RFA, but also has potential to provide guidance to the ablation procedure.

Finite Element Method

The description of the laws of physics of space- and time-dependent problems are usually expressed in terms of partial differential equations (PDEs). Most nonlinear PDEs (i.e. those with

constitutive parameters that are a function of the dependent variable) cannot be exactly solved with analytical methods. Instead, the approximation equations of PDEs based upon different types of discretization will be solved with numerical model methods [30]. Finite difference method (FDM), radial basis collocation and finite element method (FEM) are widely used numerical methods for solving numerical models and provide an approximation of the exact solution of the PDEs.

The FEM was first proposed to solve complex elasticity and structural analysis problems in civil and aeronautical engineering [31]. It has also been applied to solve the Laplace equation for potential and current distributions in order to determine the dissipated power density [32]. To solve the problem, it subdivides the special domain into smaller and simpler shapes that are called finite elements [31]. The FEM has been applied to solve problems in heat transfer, fluid flow, mass transport and electromagnetic potential. The FEM offers great freedom in the selection of discretization, both in the discretized space elements and the basis function. Another strength of the FEM over other numerical methods is that the theory of FEM has been extensively developed. These two benefits make FEM the most widely used computational method RFA modeling. Many FEM commercial software, such as ANSYS [33], COMSOL, TOPAZ3D, have been developed to obtain the solution. COMSOL Multiphysics was employed in our study to simulate and predict the tissue ablation environment with FEM.

Geometry simplification

The geometry of the electrode and surrounding tissue for an RFA problem could be very complex, which may increase the computational burden in terms of computation time and required memory resources. Therefore, when possible, it is helpful to apply appropriate simplifications to

the model geometry to reduce the computational burden, while proving model outputs that remain meaningful approximations of the physical situation. The simplifications include looking for planes or axes of symmetry which will simplify higher dimensional model into a lower one. Also, it may be helpful to implement simulations that only consider the most significant tissues which have an impact on the final ablation results.

Governing electrical and thermal equations

RFA can be modeled as a coupled electrical conduction and heat conduction problem [27]. The simulation will be divided into three distinct parts: electric field distribution, temperature distribution, and the cumulative thermal damage integral. Correspondingly, two partial differential equations governing the physical phenomenon of electrical-thermal heating are Laplace's equation and Pennes bioheat equation. Arrhenius equation is an ordinary differential equation that estimates thermal damage to tissue due to the transient temperature history at a given point.

The first part is the calculation of the electric potential (voltage) distribution which is generated by application of RF current via the electrodes. At the frequency employed in RF ablation (300 kHz – 1 MHz), the electromagnetic fields can be considered to be quasi-static and the tissue can be approximated as purely resistive [12]. The distributed heat source Q_{ext} is given by

$$Q_{ext} = \mathbf{J} \cdot \mathbf{E} \ (Eq. 1)$$

where **J** is the current density [A/m^2] and **E** is the electric field intensity [V/m]. The electric field is solved by Laplace's equation,

$$\nabla \cdot [\sigma(T) \nabla V] = 0 \quad (Eq. 2)$$

where ∇ is the gradient operator, $\sigma(T)$ [S/m] is the temperature dependent electrical conductivity of the tissue.

The second part of simulation is to determine the transient evolution of temperature throughout the tissue. The spatial distribution of temperature is solved by using a modified Pennes' bioheat equation [34],

$$\rho C \frac{\partial T}{\partial t} = \nabla \cdot (k \nabla T) + Q_{ext} + Q_{met} - Q_p \quad (Eq. 3)$$

where ρ refers to the tissue density [$kg \cdot m^{-3}$], C is the heat capacity of the tissue [$J \cdot kg^{-1} \cdot K^{-1}$], k is the thermal conductivity ($W \cdot m^{-1} \cdot K^{-1}$), T is the temperature (K), Q_{ext} is the heat source from RF electrodes ($W \cdot m^{-3}$) which is calculated q from Equation 1, Q_{met} indicates contribution of heat due to the tissue metabolic activities and is significantly smaller than the RF heat source(Q_{ext}), usually set to 0 in the model [35], Q_p is the heat loss due to blood perfusion ($W \cdot m^{-3}$), which is sometimes neglected when models are used for simulating ablations in *ex vivo* tissue.

The last part of the model is the estimation of tissue thermal damage. After heating the target zone, tissue protein starts to coagulate after reaching a certain temperature and cause tissue damage. The extent of damage induced by heating is a complex function of the time – temperature history during heating. The calculation of damage integral is computed through a well-established equation called Arrhenius equation.

$$\Omega(t) = A \int exp\left(-\frac{\Delta E}{RT(t)}\right) dt \quad (Eq. 4)$$

where $\Omega(t)$ is the degree of tissue injury, A and ΔE are called "Arrhenius parameters", A is frequency factor for the kinetic expression ($A = 7.39 \times 10^{39}/s$), ΔE is the activation energy for the irreversible damage reaction [36] ($\Delta E = 2.577 \times 10^5 J \cdot mol^{-1}$), R is the universal gas

constant ($R = 8.314\, J/(K \cdot mol)$). A tissue thermal damage integral value of $\Omega = 1$ indicates 63% of the cell damage process is complete. Similarly, a value of $\Omega = 4.6$ corresponds to 99% of the cell damage process being complete.

Equations 1-4 will be adequate to solve the electrical-thermal coupled problem, and provide an estimate of the spatial thermal damage profiles following RF ablation.

Specification of initial and boundary conditions

In differential equations, boundary conditions are a set of conditions specified at the extremes (boundaries) of the independent variables within the equations [37]. On the other hand, initial conditions specify the value of the dependent variables within transient differential equations at t = 0. Both electrical and thermal boundary conditions need to be declared before modeling.

Typically, the dependent variable of electric boundary is the electric potential V. Since the Laplace equation (Eq. 2) is a stationary equation independent of time, initial conditions do not need to be stated. The electrical boundary conditions may be specified in one of three ways: Dirichlet, Neumann, and Robin types. With a Dirichlet, the value of the dependent variable is specified, for example, a fixed voltage on the electrodes (e.g. 0 V at the dispersive electrode and $\neq$ 0 V at the active electrode). This boundary condition would be appropriate for modeling a constant voltage boundary condition, i.e. where the generator applies a fixed voltage on the electrodes, regardless of changes in tissue impedance during the ablation. A Neumann condition, meanwhile, is used to prescribe a flux, that is, a gradient of the dependent variable. A robin condition is a combination of Neumann and Dirichlet boundary conditions [38]. Conversely, RF

ablation could be delivered in a constant current way. Thus, an appropriate method for specifying the electrical boundary condition on the ablation electrodes would be a Dirichlet boundary specifying the current to be a fixed, non-zero value. Lastly, some ablation generators employ a controller to ensure delivery of constant power, by adjusting the applied voltage and/or current on the electrode surface to ensure a constant power is delivered to the tissue load. The RF generator employed for our experimental studies (see Chapter 3) operates in constant power mode. The generator records the applied voltage and current at its output terminal, and logs these values to a file. In simulation, we employed a Dirichlet boundary condition specifying the voltage at the electrode to follow the transient voltage data recorded by the generator during experiments. The adjustment of fixed voltage will result in an approximate constant power in simulations. This approach was employed since we did not have access to the generator's proprietary control algorithm used to ensure constant power delivery in practice.

Electric insulation boundary condition is applied to non-conducting surface with equation $\mathbf{n} \cdot \mathbf{J} = 0$; where **n** is the unit vector normal to the surface and **J** is current density on the surface. This means there is no current can flow through the boundary and that the electric potential is discontinuous across the boundary

The dependent variable for the thermal models is the temperature T. The initial temperature value is determined from the initial tissue temperatures during experimentation. The thermal boundary condition has two types: specified temperature and specified heat flux. The former is of a constraint type and prescribes the temperature at a boundary: $\mathrm{T} = \mathrm{T}_{amb}$, while the latter specifies the inward heat flux: $-\mathbf{n} \cdot \mathbf{q} = \mathbf{q}_0$; where q is the conductive heat flux vector, q_0 is inward heat flux vector normal to the boundary and n is the normal vector of the boundary. We employed the initial condition of specified temperature in our modeling.

Thermal insulation (i.e. no heat flux) is applied to outside surface with equation $\mathbf{n} \cdot (k\nabla T) = 0$; where n is the unit vector normal to the surface, k is the thermal conductivity, and ∇T is the temperature gradient. This equation shows the temperature difference across the boundary must be zero and no heat can transfer across the outside surface.

Material parameters

For *ex vivo* simulations, equations 1-3 require the specification of four material properties within all domains: mass density (ρ), electrical conductivity (σ), thermal conductivity (k), and heat capacity (c). These parameters vary in different organs and tissue types and have their own characteristics. All these material data are taken from previous scientific literature and listed below. Table 2-1 lists the baseline material properties employed for all simulations. Note that the tissue domain used properties of liver tissue, since benchtop experiments employed for validating the model were conducted in liver, an established experimental model for characterizing thermal ablation technologies. As described in later sections, tissue electrical conductivity and heat capacity were modeled as being temperature dependent.

	Density (ρ) Kg/m^3	Electrical Conductivity(σ) S/m	Thermal Conductivity(k) W/m·K	Heat Capacity (Cp) J/Kg·K
Liver tissue	1060	0.36	0.51	3600
Catheter	70	10^{-5}	0.03	1045
Electrode	21500	4×10^7	71	132

Table 2-1 Material physical properties employed in simulations.

In most cases, the tissue mass density and thermal conductivity varies slightly, while electrical conductivity and heat capacity are influenced by temperature. Tissue electric conductivity increases with a temperature coefficient of 0.7%/°C below 100 °C. Our procedure also includes a temperature of nearly 100 °C. The water in tissue changes to gas and non-linear phenomena occurs at temperatures near ~100 °C. Tissue vaporization and desiccation need to be taken into account since they considerably alter the impedance at the electrode-tissue interface. The electrical conductivity (σ) has a rapid drop by a factor of 10000 over a 2 °C interval, due to the tissue water vaporization [39]. In order to balance computational time, the electrical conductivity was kept constant between 100°C and 105 °C , and the slope σ is reduced to 5 between 105 °C and 110 °C [40]. Figure 2-1 shows the electrical conductivity temperature dependency previously reported in the literature [27], and the simplified electrical conductivity approximation applied in our simulations.

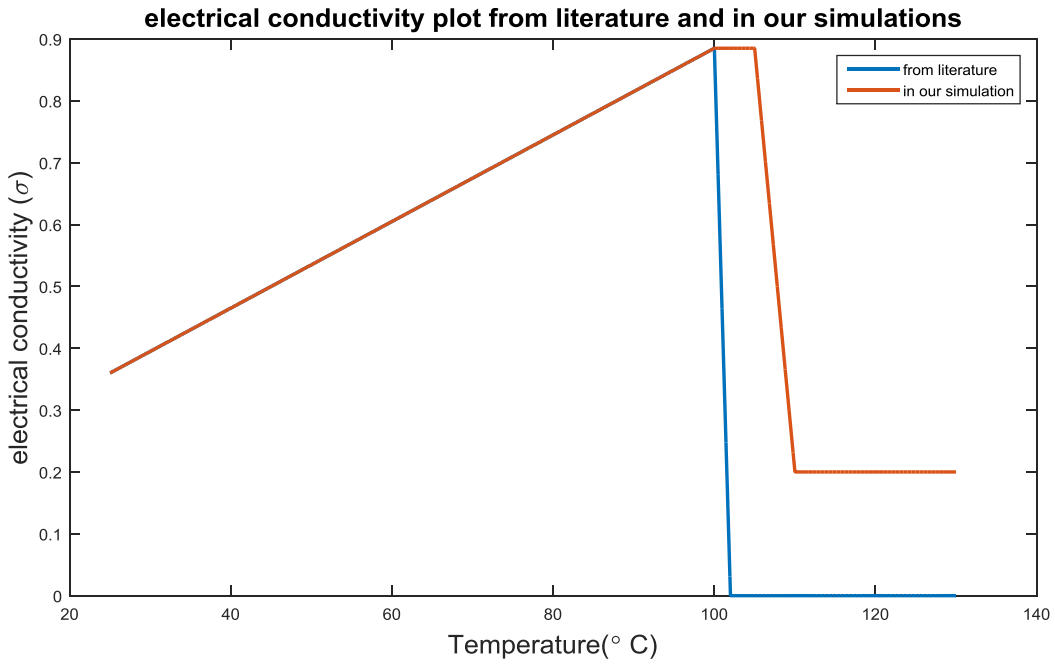

Figure 2-1 Literature tissue electrical conductivity and our approximation tissue electrical conductivity plot.

Heat capacity is also considerably influenced by tissue vaporization. At T=100 °C, the latent heat (L) is required to convert liquid water to water vapor. C(T) is the specific heat capacity as a function of temperature and includes the latent heat L for evaporation of the relative water content in the tissue at this time [41]. The equation of heat capacity around 100°C is shown below. Due to computation time, we assume the temperature range over which tissue water vaporizes was approximated as $\Delta T = 2.5$ ℃ as compared to $\Delta T = 1$ ℃ which has been employed in some studies in the literature [27].

$$C(T) = C + L \cdot \frac{\exp(-\frac{(T-100)^2}{\Delta T^2})}{\sqrt{\Delta T^2 \pi}}$$

where C(T) is the heat capacity at this temperature, C is the original heat capacity, L is the specific latent heat for water ($L = 2.2 \times 10^6\ J/Kg$), T is temperature, ΔT is the temperature region where the liquid-to-gas transition occurs.

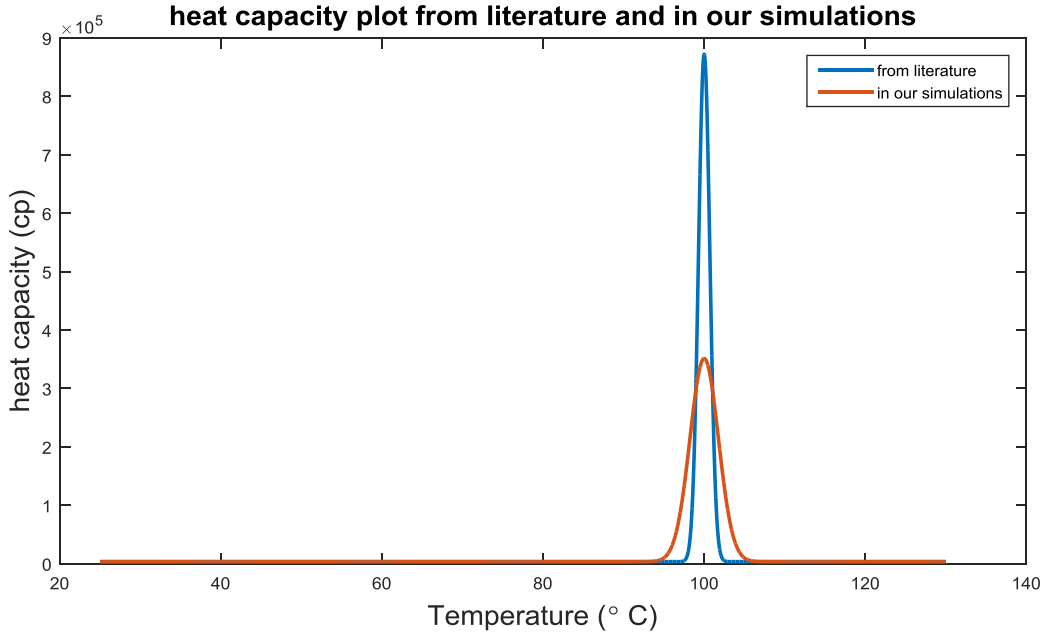

Figure 2-2 Literature tissue heat capacity and our approximation tissue heat capacity plot.

Post processing of model outputs

The output values of computational models of RFA include thermal and electrical parameters, such as temperature, heat flux, electrical potential, and current density. Although the Arrhenius thermal damage integral provides a more accurate representation of the cell death process, an isothermal contour/boundary is often used as a surrogate to estimate the extent of the thermal ablation zone (in the literature, often also referred to as the thermal lesion). The size and volume of the ablation zone could be measured and this is an important index for comparison against the geometry of the desired target. Moreover, the discoloration observed during ablation experiments in tissue after it is heated to a certain temperature (50 – 60 °C) allows us comparing the simulation isothermal contour line with experiment results.

Chapter 3 - RF ablation computational model and experimental validation in *ex vivo* tissue

The computational models employed in this thesis have been previously developed and experimentally validated for various applications. Nevertheless, since this was the first use of RF ablation computational models in the KSU Biomedical Computing and Devices Lab, we sought to establish an experimental validation for our models. In this chapter, we report on single pair bipolar RF ablation experiments in fresh bovine liver and compare to the corresponding FEM simulation with a similar geometry. Application of the computational model for investigating RFA devices and energy delivery strategies for rhinitis treatments is described in Chapter 4.

Bipolar RFA experiments in *ex vivo* liver tissue

All ablation in the experiments were performed with a prototype RFA generator developed by Dean Miller Associates (Menlo Park, CA). The generator provides constant RF power to the electrodes at 460 kHz. The user can select the applied power level within the range 0.5 W - 30 W, in increments of 0.5 W. When the resistance between the electrodes exceeds 512 Ω., applied power is automatically reduced to 0 W and the ablation procedure is terminated. Alternatively, the user can manually terminate the procedure at any time. The system records resistance, current, voltage, power measurements between electrodes during ablation procedure every 0.031 s.

For this experiment, a simplified electrode geometry was selected to ensure ease of geometric representation within the COMSOL modeling environment. Figure 3-1 shows a diagram of the needle ablation electrodes used in this experiment. The electrodes were implemented with

25 mm stainless steel hypodermic tubing, with the proximal 17 mm with insulating hear shrink tubing. The diameter of conducting tip is 1.25 mm and the diameter of insulated part is 2.19 mm. The two needles with an 8 mm uninsulated tip were inserted into the liver tissue. The distance between two electrodes was 7.15 mm. This represents a bipolar RFA configuration. The setup of the ablation system is shown in figure 3-2.

Figure 3-1 Single needle ablation electrode probe geometry.

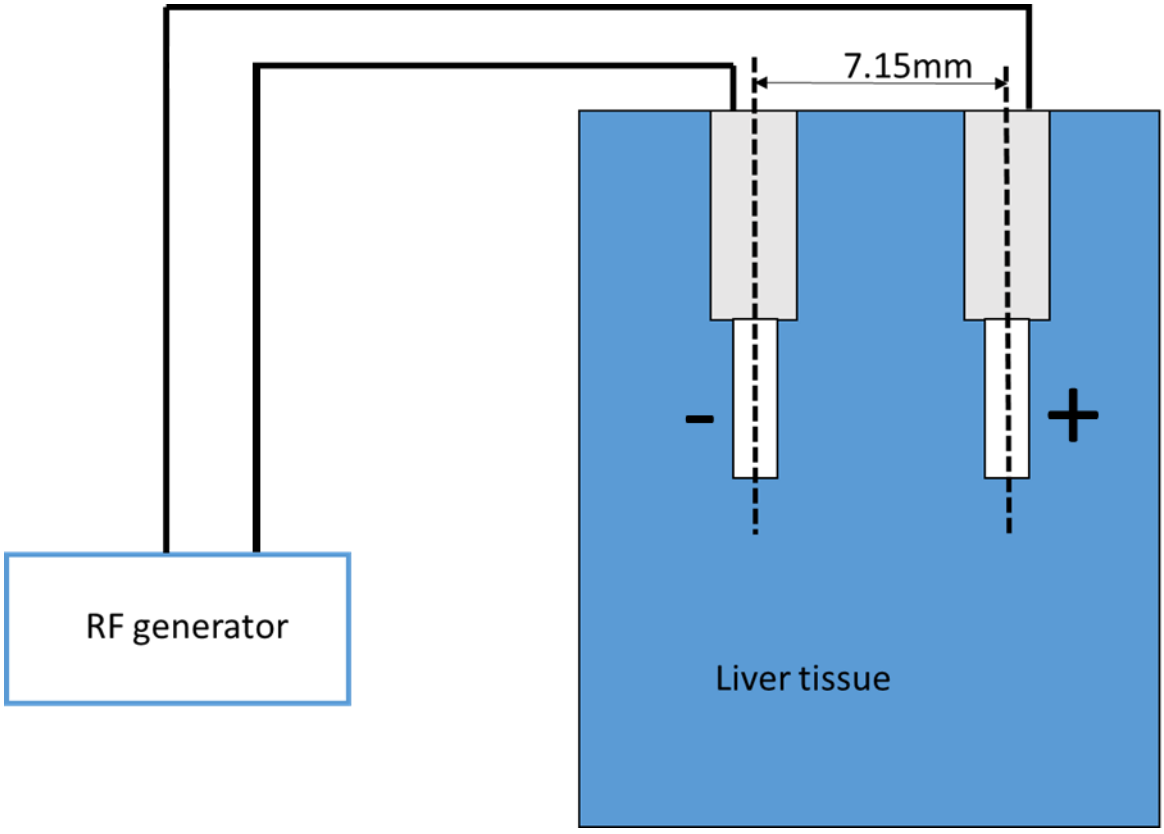

Figure 3-2 Experimental setup for bipolar RF ablation validation experiment in *ex vivo* liver.

Experiments were performed in freshly excised bovine liver sections. Livers were obtained from a local slaughterhouse and transported to our lab in plastic bags placed on ice. The liver tissue was warmed up to ~28 °C before ablation by placing sectioned liver pieces within thin sealed plastic bags placed within a water bath. A plexiglass template with two drilled holes was applied to maintain a fixed distance between the two probes. We inserted the needle into the center of liver tissue through the template holes. The sample was ablated with 9 W applied power until we turned generator off when the resistance between probes was higher than 250 Ω. The probes were then removed and the tissue was bisected immediately to expose the lesion. The discoloration of tissue around probes indicated ablated region. The healthy tissue stayed red while ablated zone was in white color. We took measurement on the width and depth of the macroscopically pale ablated zone. This procedure was repeated three times with same power and terminate condition.

Bipolar RFA simulations

In simulation, we built a three-dimensional geometric liver model with electrical current and joule heating multiphysics in COMSOL, as described in Chapter 2. Figure 3-3 shows the model geometry. Both electrodes were positioned in the center of a block tissue model that is 50 mm in height, 42 mm in width and 42 mm in depth to mimic the experimental settings. The diameter of catheter and electrode is 1.24 mm

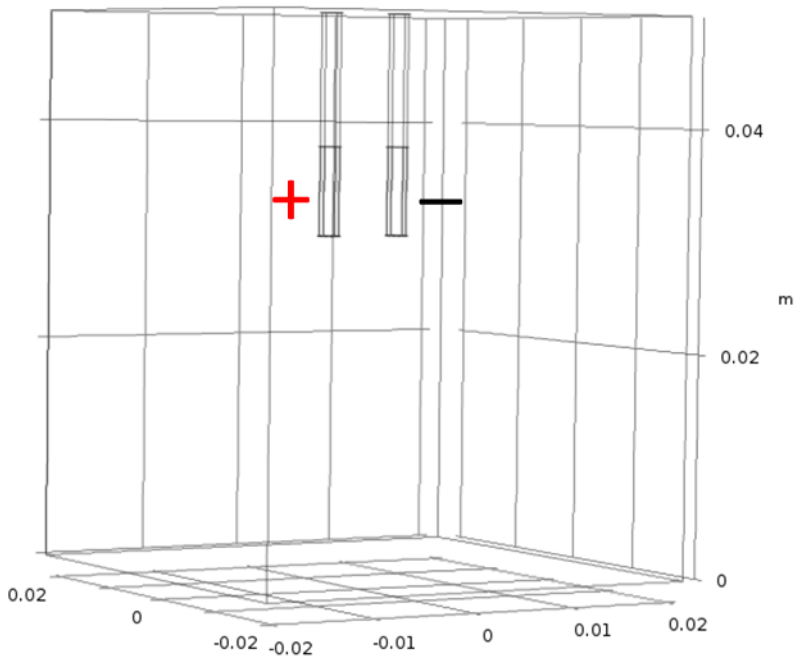

Figure 3-3 Model geometry mimicking experimental setup for bipolar ablation validation experiments conducted in *ex vivo* liver.

For electrical boundary condition, a fixed source voltage (V) is applied to the conducting tip surface of one needle while the outer surface of the other needle was specified as 0 V, serving as a return. The amplitude of the applied voltage was adjusted at each time step to match the voltage applied at the electrode boundary by the generator (data taken from the generator's log file). In this way, by adjusting potential voltage, the total amount of power delivered in the tissue should remain at 9 W as specified by the generator. Figure 3-4 shows the voltage applied to the active electrode in the computational model. Electrical insulation boundaries are applied to the outer surface of the model. The electrical equation are calculated in all domains except the inside of electrodes (i.e. the model was implemented to assume uniform potential across each electrode, which is reasonable due to their high electrical conductivity).

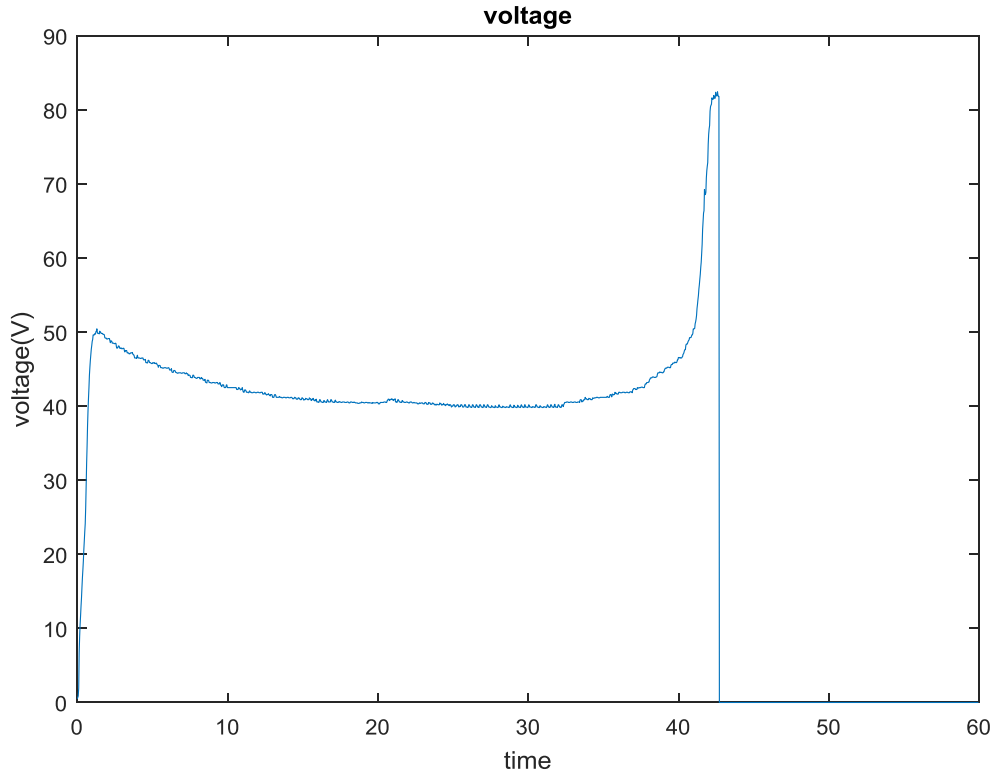

Figure 3-4 Experimentally applied voltage at the active electrode during bipolar ablation in *ex vivo* tissue.

For the thermal model, the initial temperature is specified as 28 °C, equivalent to the tissue temperature in experiment. A thermal insulation boundary condition (i.e. no heat flux) is applied to the outer tissue surfaces. The material properties are listed in Chapter 2.

Tetrahedral mesh elements were employed for spatial discretization within the simulation domain. A non-uniform mesh was specified with finest mesh density in regions such as electrodes, where thermal and electrical gradients are expected to be steep, and relatively larger mesh elements in other regions, such as tissue away from electrodes. The total number of degrees of freedom within the model was 238601. The model simulates a 60 s ablation with 0.5 s time step intervals. The actual time steps taken by the solver in time iteration are regulated by the solver itself using an implicit time stepping scheme. For the duration of the simulation, the resistance (R), the power

(P), the temperature (T) and 50 °C temperature contour are calculated. The simulation was implemented on a computer with a dual Intel Xeon E5-2665 Processor with 64 GB RAM. The simulation time was approximately 1.5 h.

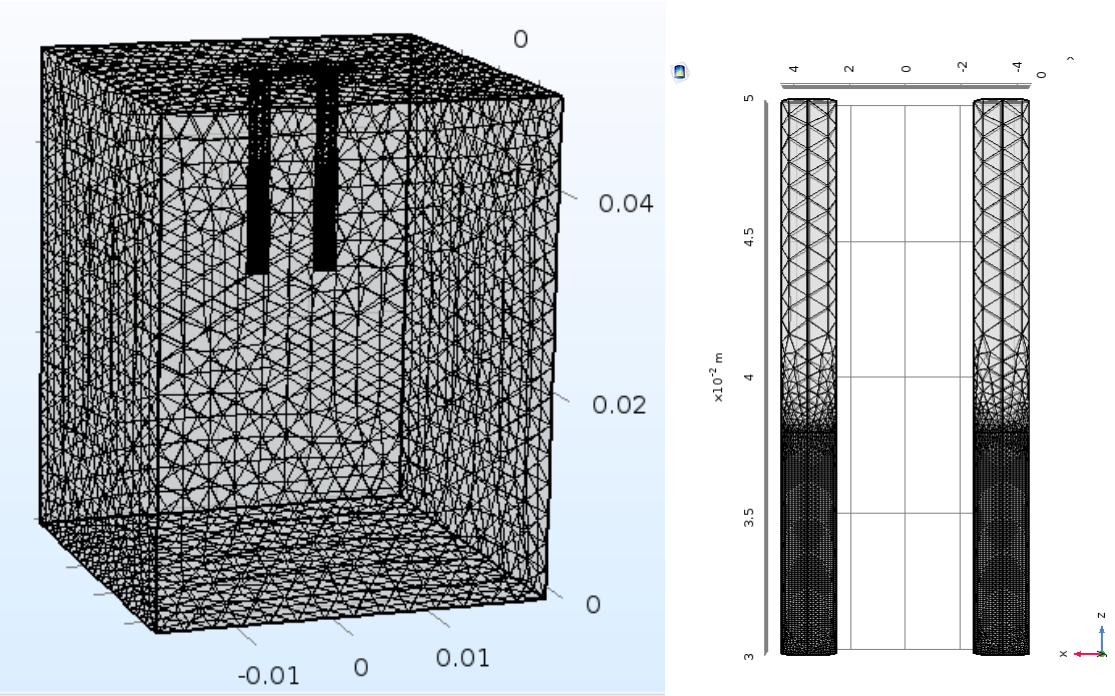

Figure 3-5 Meshing of bipolar electrodes and tissue using tetrahedral elements.

Results

Experimentally observed ablation zone dimensions and time at which the ablation was terminated are listed in Table 3-1, following $n = 3$ experiments under similar conditions. The total ablation time was around 40 s. The ablation zone size was estimated by taking measurements of the region of visibly discolored tissue after bisecting the tissue sample. Figure 3-6 depicts the bisected liver tissue following RFA for all three experiments, with ablation zone width and depth labeled.

	Ablation time	Lesion size (width, depth)
Experiment 1	43 s	15 mm × 14 mm
Experiment 2	41 s	14 mm × 17 mm
Experiment 3	42 s	15 mm × 17 mm

Table 3-1 Experiments' ablation time and lesion size.

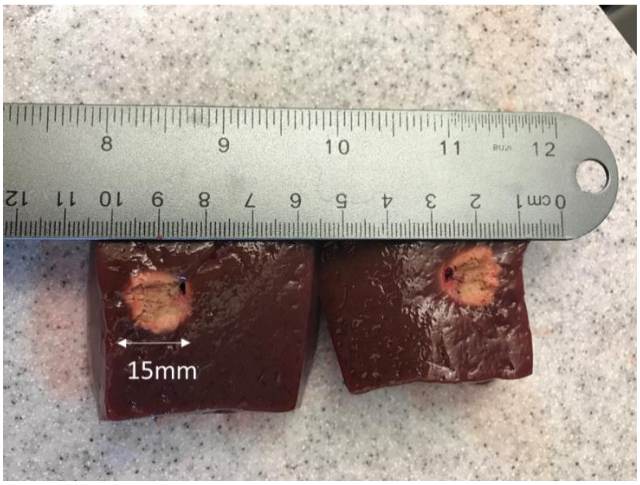

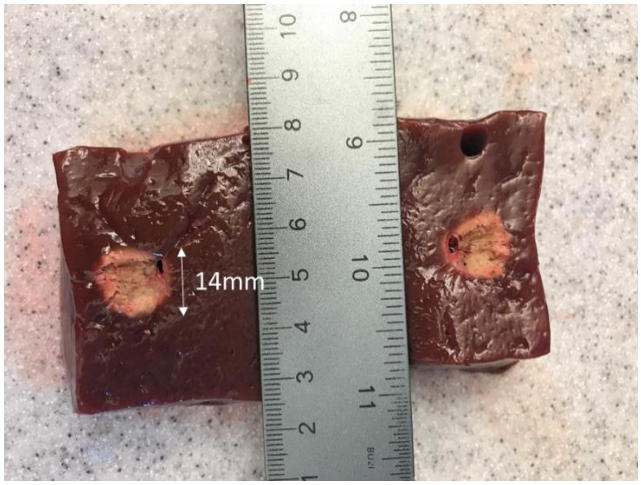

(a) Experiment 1

(b) Experiment 2

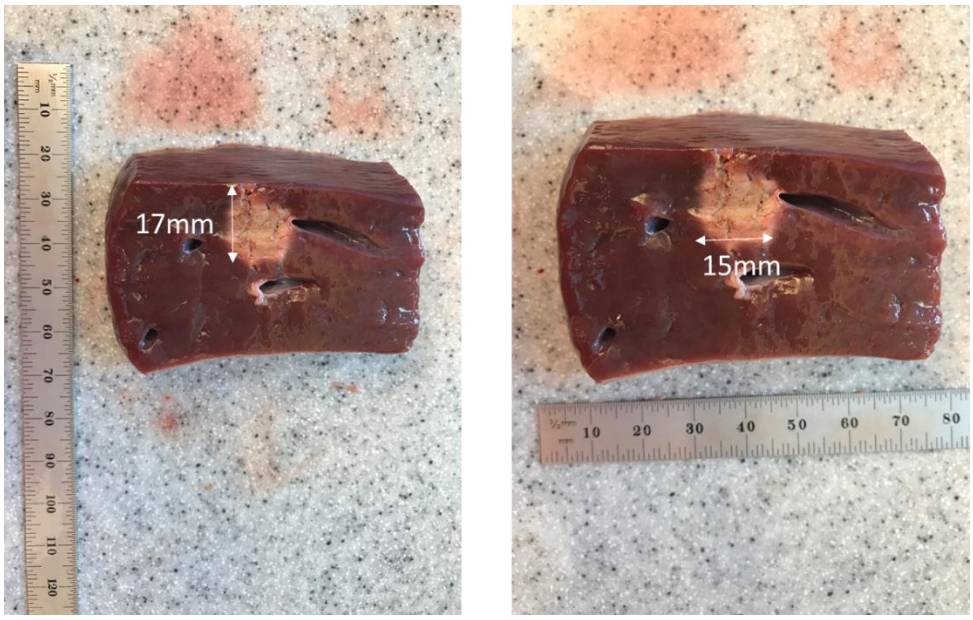

(c) Experiment 3

Figure 3-6 Ablation lesions from experiment 1, 2, and 3.

The 50 °C contour is a commonly used isotherm for estimating thermal ablation zone dimensions [35]. We compared the computed 50 °C contour to the discoloration lesion zone from experiment. Figure 3-7 shows the temperature distribution and figure 3-8 (a) illustrate a 3-D isothermal surface plot of a RFA zone with temperature exceeding 50 °C. The ellipsoid RF ablation zone is created measuring 14 mm in width and 13.1mm in depth in figure 3-8. This indicates a close agreement between the computational lesion size and the experimental results.

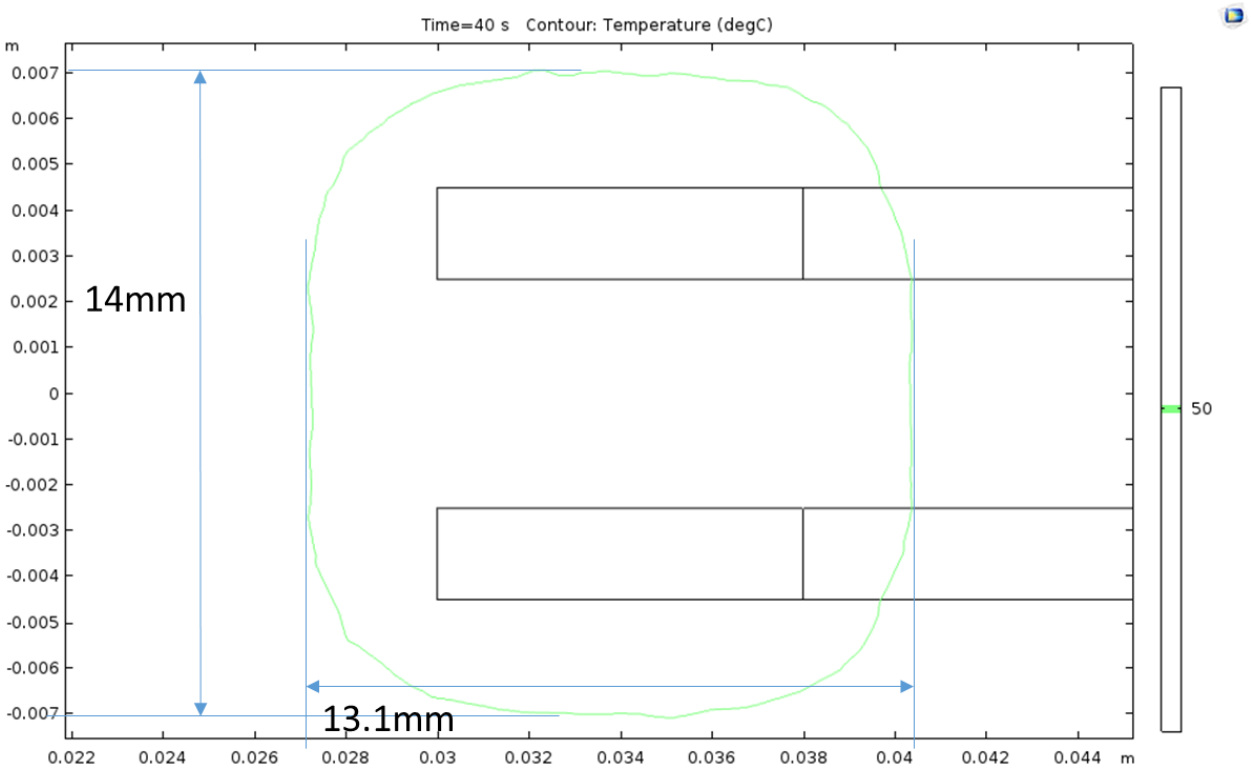

Figure 3-7 50 °C lesion contour in our simulation.

From experiment 1, the applied power, applied voltage, and measured impedance between two electrodes are plotted below in figure 3-8 (a) – (c). The initial resistance between the electrodes was 270 Ω and slowly dropped down to 190 Ω over a period of 37 s. After 37 s, tissue impedance had a sudden increase to over 400 Ω. At this point, power was terminated manually. We hypothesize the reason for this sudden increase is that the tissue water began to evaporate and turn into gas after heating to 100 °C, and the impedance at the electrode-tissue interface rose due to the electrically insulating vapor, as well as formation of charred tissue. In simulation, the applied voltage was adjusted by using the set power (9 W) and measured resistance with the equation :$V_{rms} = \sqrt{P \cdot R}$.

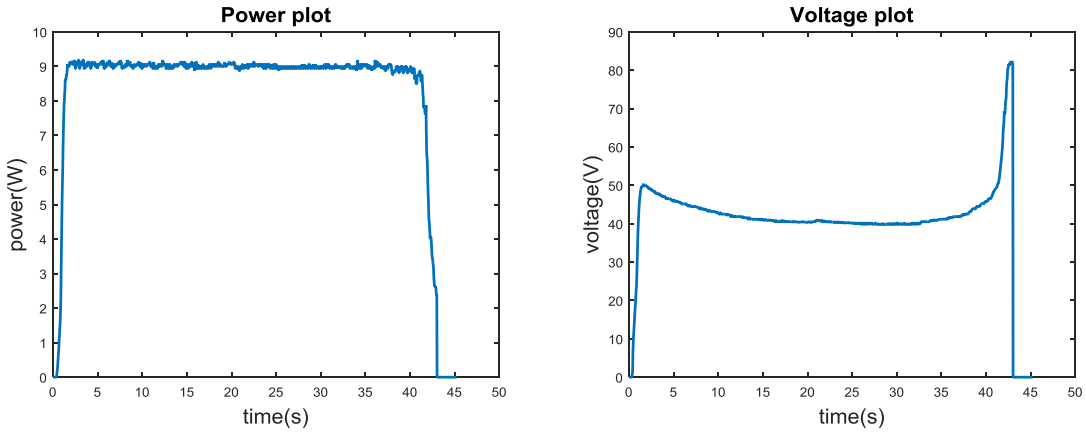

(a) (b)

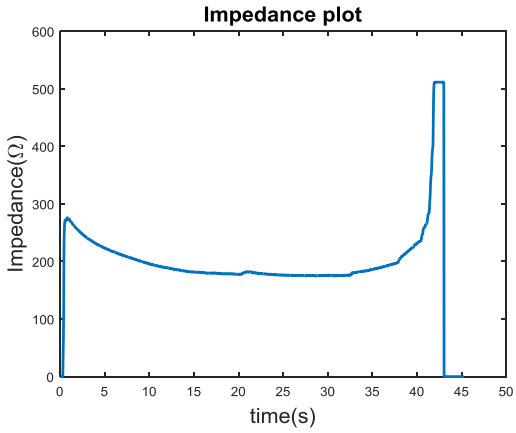

(c)

Figure 3-8 Applied power, voltage, and measured impedance plot during bipolar RF ablation in *ex vivo* liver.

Figure 3-9 illustrates the corresponding applied power (from 8.27 W to 10 W with a mean of 8.89 W, red solid line in figure 3-9) from simulation and the fixed power in one experiment from generator's log file (blue solid line in figure 3-9).

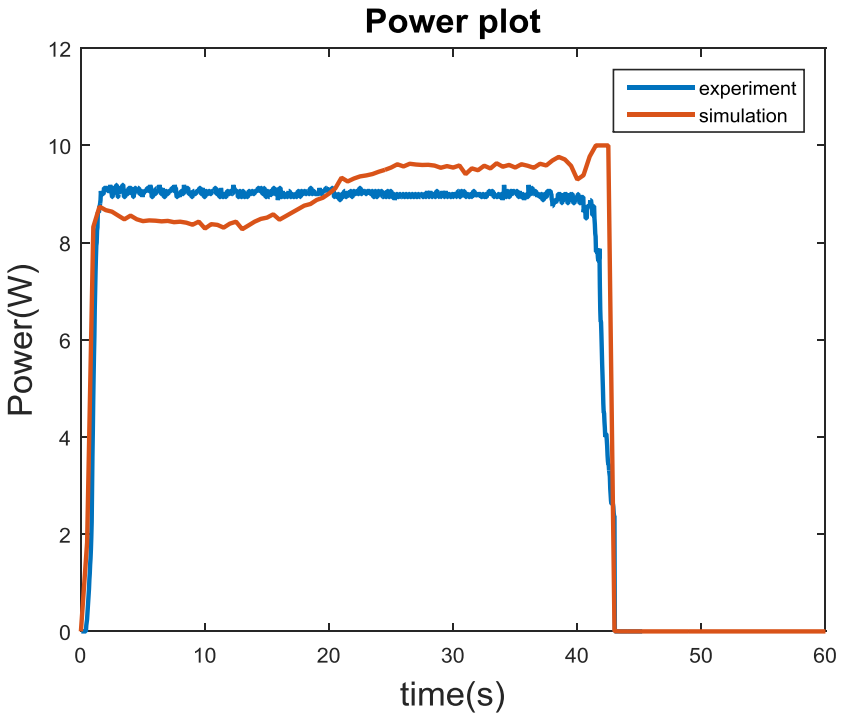

Figure 3-9 Comparison of experimentally applied power and simulation calculated power during bipolar RF ablation in *ex vivo* liver.

Figure 3-10 compares the transient changes in resistance at the tissue-electrode interface during both experiment and simulation. In experiment, the impedance ranges from 165 Ω to 310 Ω with an average of 206 Ω. The correlation coefficient (*R*) between impedance from experiment and simulation is 0.916. Since it is rather close to 1, we can conclude that the variables are positively linearly related. Figure 3-11 shows a scatter plot of impedance from experiment and simulation.

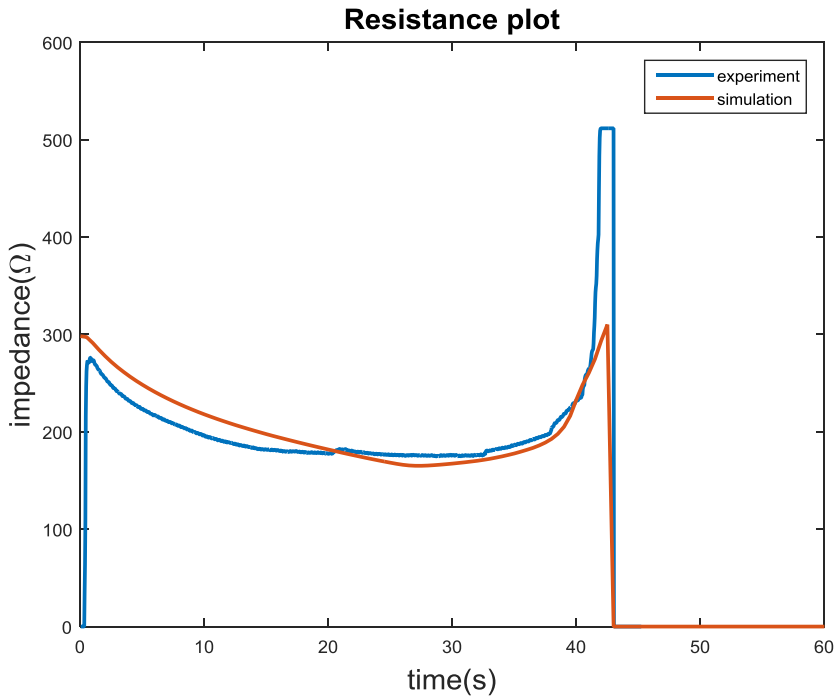

Figure 3-10 Plot of impedance from experiment and simulation versus time during bipolar RF ablation in *ex vivo* liver.

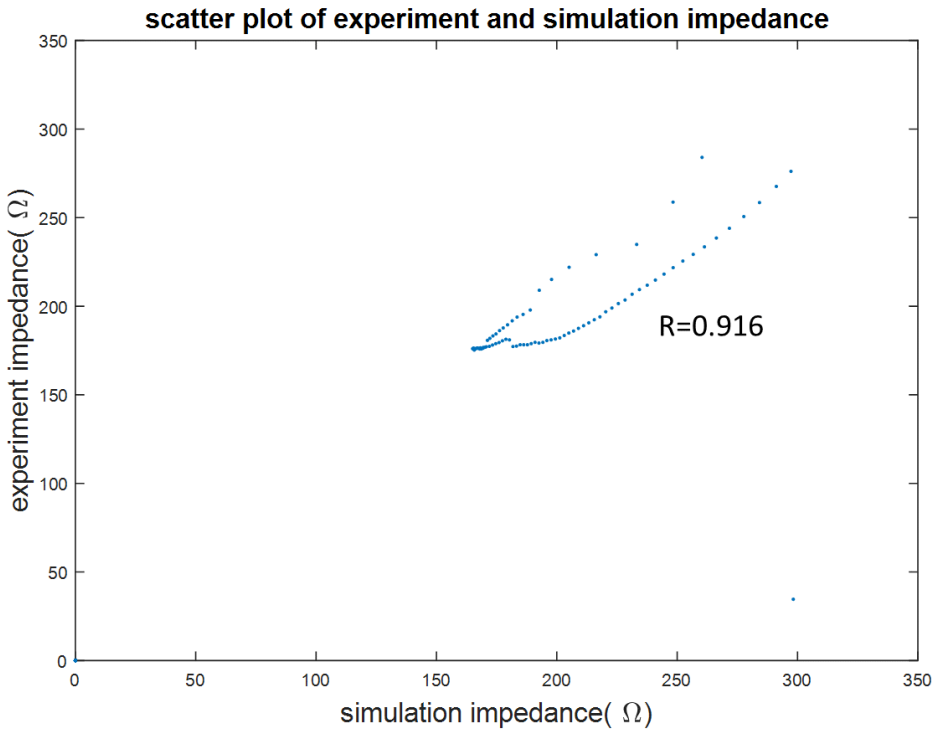

Figure 3-11 Scatter plot of experiment and simulation impedance.

By comparing the lesion size, applied power, measured impedance between experimental and computational results, we conclude that there is a positively high correlation between experiments and simulations. We could use the simulation results to predict the level and area of potential damage created with bipolar RF electrodes.

Chapter 4 - Three-dimensional finite-element analyses for Neurent basket electrode: influence of electrode size and duty cycle

In this chapter, we implemented computational simulations to predict tissue lesion formation with a custom multi-element basket RF ablation electrode. The objective of these studies was to investigate the effects of basket wire diameter and wire length, and applied RF power duty cycle on ablation zone formation during the ablation. An egg white experiment and its simplified FEM models were developed to compare tissue lesion size. Three-dimensional electrical FEM models under constant current density and constant current were simulated with different electrode wire diameter and length. Thermal-electrical FEM models with fixed voltage were built to evaluate the duty cycle's effect.

Neurent basket electrode

The Neurent basket electrode is a handheld bipolar RF probe designed for use in otorhinolaryngology (ENT) surgery developed by Neurent Medical [42]. The probe is shown below in figure 4-1. The probe includes a handle, a shaft and treatment tip. The treatment tip compromises eight arches with five pairs of bipolar electrodes on each arch. Each arch includes two parallel semicircle arcs. The distance between the centers of parallel arcs is 0.25 mm. The diameter of the probe is 7 mm. The diameter and length of electrode are 0.2 mm and 1 mm. The inter-spacing between one pair electrodes is 0.75 mm. The RF probe is connected to the RF generator mentioned in Chapter 3 via a flexible customized cable.

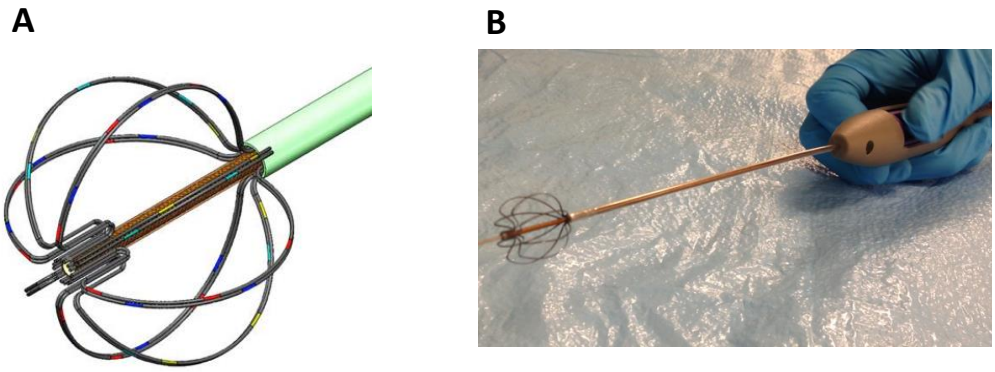

Figure 4-1 Neurent basket electrode [42].

The straight RF probe is inserted into patient's nostril guided by a distance indicator on the probe handle. Once reaching the marker, the surgeons deploys the probe into a basket and commences the ablation. The basket electrodes will be retracted after ablation before being withdrawn from the nostril.

Neurent basket electrode egg white validated experiment

Experiment

The experiments were performed in fresh egg white. Egg white was directly separated from whole eggs which were bought from local market. The eggs were placed in room temperature for half hour. The temperature of egg white was ~28 °C before ablation. A 50 mL beaker was filled with egg white. The Neurent basket electrode was inserted into the center of egg white. With customized connection cable, electrodes on 5 arcs were used during ablation procedure. The egg white was ablated with 9W applied power and was stopped manually until the resistance between electrodes exceeded 250 Ω. The experiment was repeated three times. The setup of egg white

experiment is shown below, in figure 4-2. Coagulation of egg white protein is the process of conversion of the liquid egg to a solid or semisolid state, usually accomplished by heating [43]. Egg white coagulates at 60 °C which is near to the tissue coagulation temperature (i.e. 50 °C in our study) [44]. The main advantage of egg white is its property of changing opacity and color, from a translucent clear to an opaque white, during coagulation [43]. Also, egg white can guarantee the maximum contact area at electrodes-tissue (i.e. we consider egg white as a special tissue here) interface due to the fluidity.

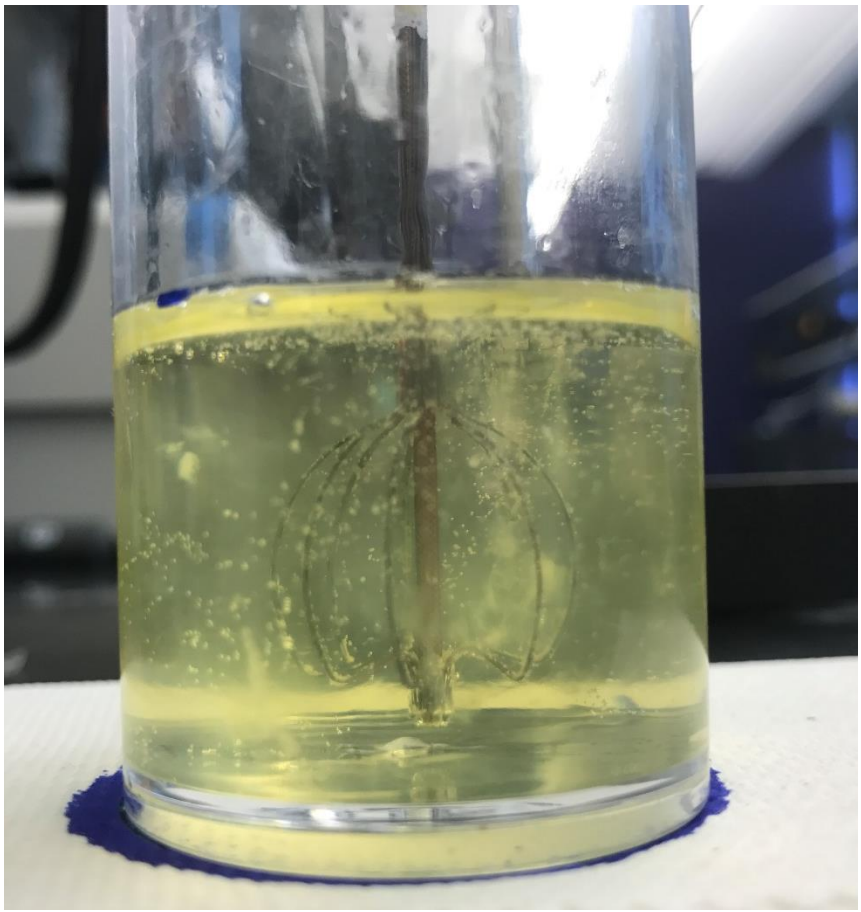

Figure 4-2 Egg white experiment setup.

Simulation

In simulation, we built a three-dimensional geometric egg white model with electrical voltage and joule heating Multiphysics in COMSOL. Figure 4-3 shows the geometry used in this model. One simplified arc with five pairs of electrodes was positioned in the center of a block egg white model with size of 10 mm × 12 mm × 20 mm .

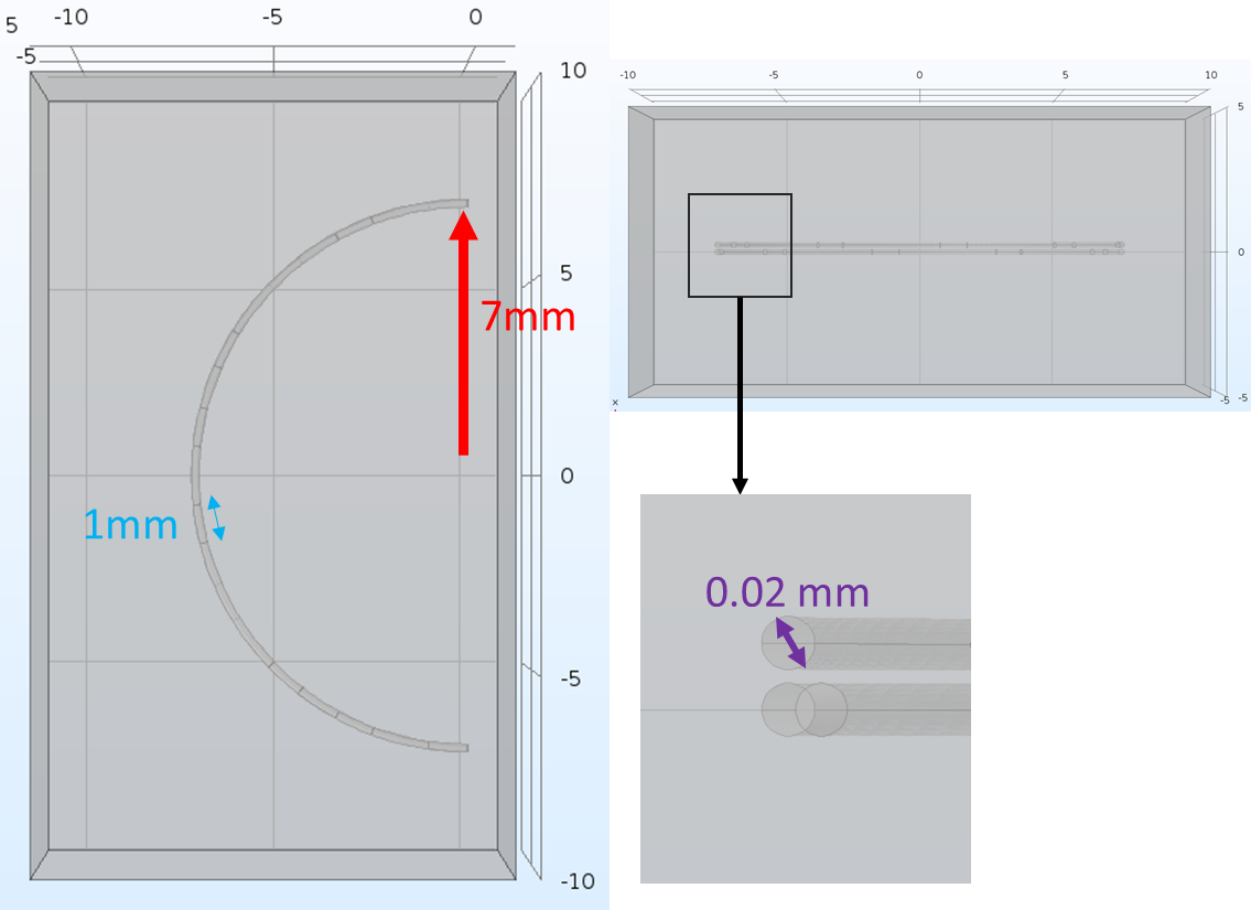

Figure 4-3 Model Geometry.

Instead of applying adjusted voltage to match the voltage applied in experiment, we noticed the voltage during the experiment ablation maintained around 20 V. Therefore, for simplification, 20 V is supplied to the conducting tip surface of the red electrode in figure 4-4 and 0 V is specified

to the outer surface of the black electrode as electrical boundary condition. For thermal boundary condition, the initial temperature is 25 °C. Thermal insulation boundary condition is applied to the outer surfaces of the block tissue.

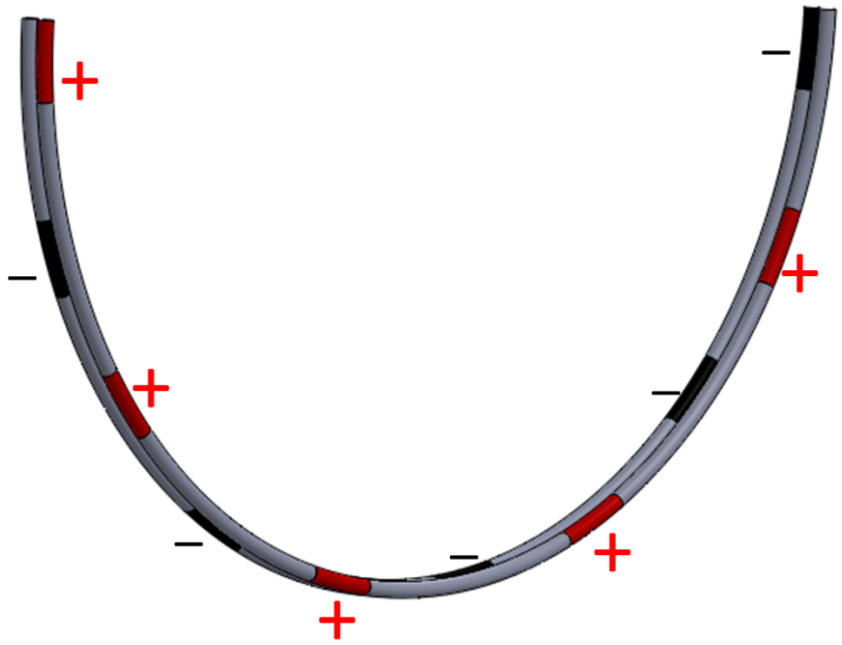

Figure 4-4 Electrical boundary condition applied to electrodes.

The material properties are listed in Table 4-1.

	Density (ρ) Kg/m^3	Electrical Conductivity (σ) S/m	Thermal Conductivity (k) W/m•K	Heat Capacity (Cp) J/Kg•K
Egg white	1027.55	0.6389	0.1588	3570
Catheter	70	10^{-5}	0.03	1045
Electrode	21500	4×10^{7}	71	132

Table 4-1 Egg white experiment material properties.

Tetrahedral mesh elements were established for all domains. Finer mesh density at regions where seemed to have steep changes, such as electrodes, and relatively coarser mesh size in other regions. The model simulates a 300 s ablation with 1 s time step intervals. The total number of degree of freedom was 520864. The simulation was implemented on a computer with a dual Intel Xeon E5-2665 Processor with 64 GB RAM. The total running time is 41 minutes.

Results

The sizes and shapes of lesions from experiments is shown in figure 4-5. The ablation times for experiment 1-3 are 5 m 7 s, 6 m 53 s, and 6 m 34 s.

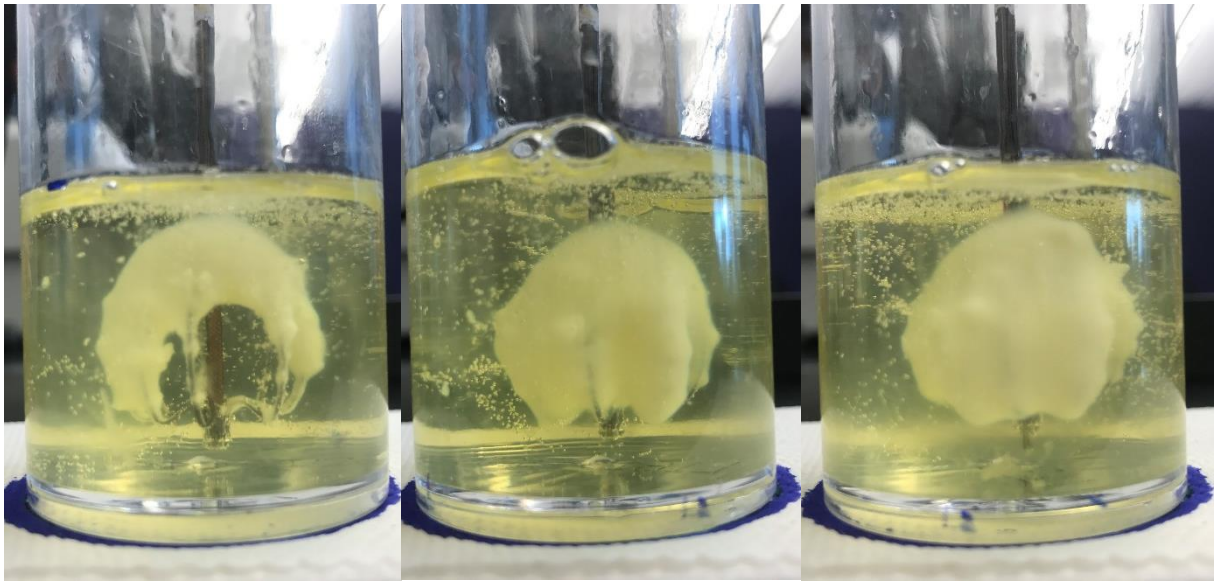

Figure 4-5 Egg white experiment results.

The lesion created from FEM simulation is shown figure 4-6. A 60 °C contour is used for estimating thermal ablation zone dimensions, as egg white coagulates at 60 °C.

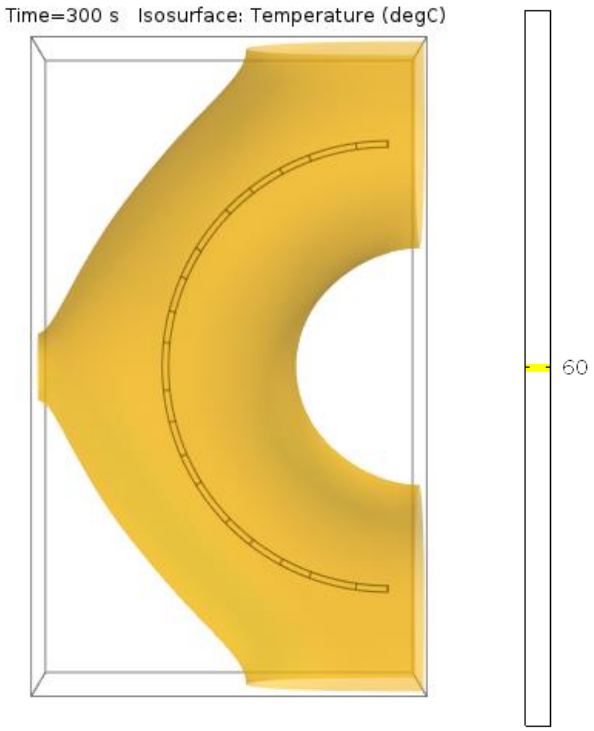

Figure 4-6 60 °C lesion contour at 300 s in FEM model.

Lesion produced during experiments appear to be smaller than the lesion predicted by FEM model. Egg white is a convenient tool for real-time visualization of heat lesion. However, the convection of egg white carries more heat away. These part of heat is supposed to help in growing larger lesion. Also, the heterogeneity of egg white makes it difficult to repeat in experiments [45]. Convection and heterogeneity explain the unusual characteristics of egg white lesions are not predictable by computer simulations [46]. But we believe that our findings on the geometry of lesion size from experiment will be helpful in planning RF device design.

Influence of electrode size on ablation zone profiles

Simulation

We employed the electrical FEM models with the change of electrode diameter and length under constant normal current density and constant current. For simplification, we applied electrical FEM model alone, instead of thermal-electrical FEM model. Typically, thermal-electrical FEM model will directly provide results of temperature profiles and lesion growth with time. However, this is also considerably more time consuming and requires larger computational resources. With electrical FEM models, current density profiles provide some insight into the changes in resistive heating patterns that can be anticipated from different electrode geometries. Figure 4-7 compares temperature profiles from thermal-electrical FEM models (electrode size D=0.3 mm L=1 mm and D=0.5 mm L=1 mm) with current density profiles from electrical FEM models with same geometry. The iso-thermal contour and iso-current density contour have similar shapes and sizes.

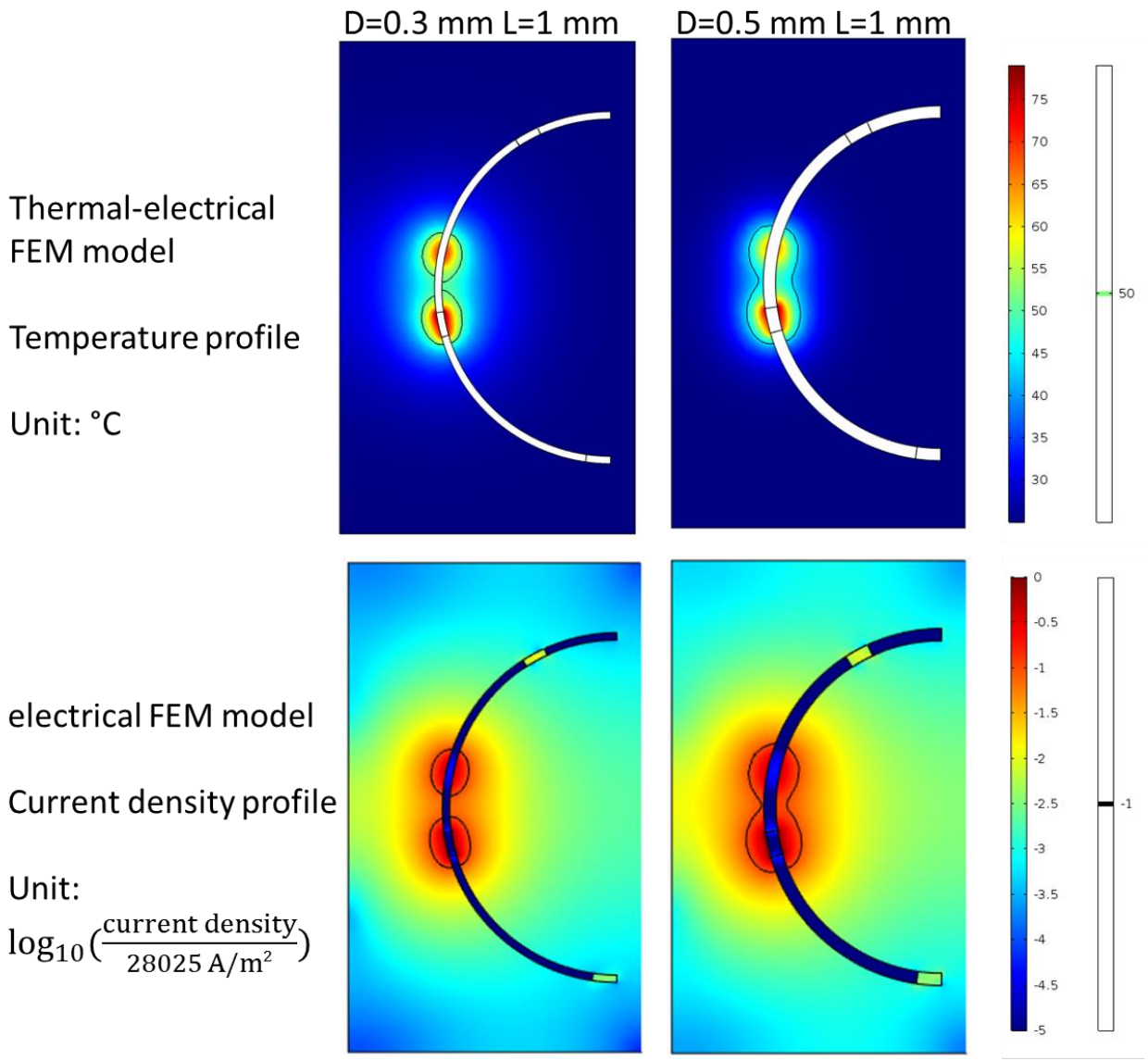

Figure 4-7 The comparison between temperature profiles and current density profiles.

One fully-deployed probe arch is placed in a rectangular tissue block. The probe arch is simplified as two parallel semicircle arc. The distance between the parallel arcs is 0.05 mm. There are three pairs electrode on each probe arch.

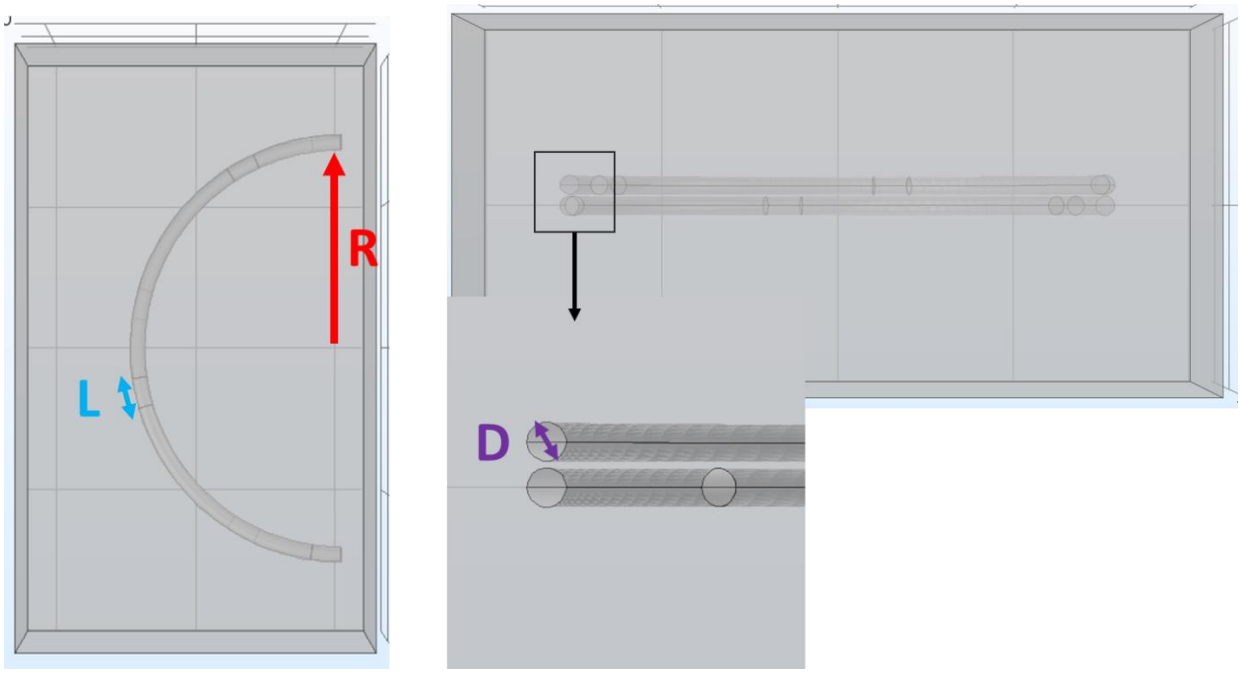

Figure 4-8 Simulation geometry with variable of electrode size labeled.

To determine the effects of the electrode size on the lesion formation, we modeled the electrode diameter with 0.1 mm, 0.3 mm, 0.5 mm, 0.7 mm and 1 mm and electrode length with 0.75 mm, 1 mm, 1.5 mm, 2 mm, 3 mm and 5 mm. The radius of electrode arc is 7 mm with electrode length 0.75 mm, 1 mm, 1.5 mm and 2 mm. We employed arcs with radius 12 mm for electrode lengths 3 mm and 5 mm to accommodate the larger electrode lengths, while maintaining the same number of electrodes as with the previous simulations. The space between each electrode in a pair is maintained at 1mm and the space between successive pairs of electrodes is adjusted for different electrode lengths. Table 4-2 below lists the electrode size combinations that were simulated. The material properties from Chapter 2 were employed in these simulations.

R=7mm	L=0.75 mm	D=0.1 mm	D=0.3 mm	D=0.5 mm	D=0.7 mm	D=1 mm
	L=1 mm	D=0.1 mm	D=0.3 mm	D=0.5 mm	D=0.7 mm	D=1 mm
	L=1.5 mm	D=0.1 mm	D=0.3 mm	D=0.5 mm	D=0.7 mm	D=1 mm
	L=2 mm	D=0.1 mm	D=0.3 mm	D=0.5 mm	D=0.7 mm	D=1 mm
R=12mm	L=3 mm	D=0.1 mm	D=0.3 mm	D=0.5 mm	D=0.7 mm	D=1 mm
	L=5 mm	D=0.1 mm	D=0.3 mm	D=0.5 mm	D=0.7 mm	D=1 mm

Table 4-2 Simulated electrode size combinations for the Neurent basket electrode.

In this study, either constant normal current density or constant current boundary conditions were applied to the electrodes. An experiment in egg white was done under 9 W power. In this experiment, 25 pairs of electrodes (i.e. 5 arcs) were used and the total current applied was 0.44 A. Since each electrode is connected in parallel, the current flowing between each pair would be 0.0176 A, assuming homogeneity of the egg white. Normal current density equals to the current divided by current surface area. The diameter is 0.2 mm and length is 1mm with one cylinder electrode. Finally, the normal current density is 28025 A/m^2 during egg white ablation experiment. This value is applied as a normal current density boundary condition in simulations. For the constant current simulations, the normal current density changes as a function of electrode surface area. The current on the electrode is maintained at 0.44 A while the diameter and length change. For both constant normal current density and constant current ablation models, the normal current density is applied on the one electrode (in red color) and zero potential is applied on the adjacent electrode (in black color), shown in figure 4-9.

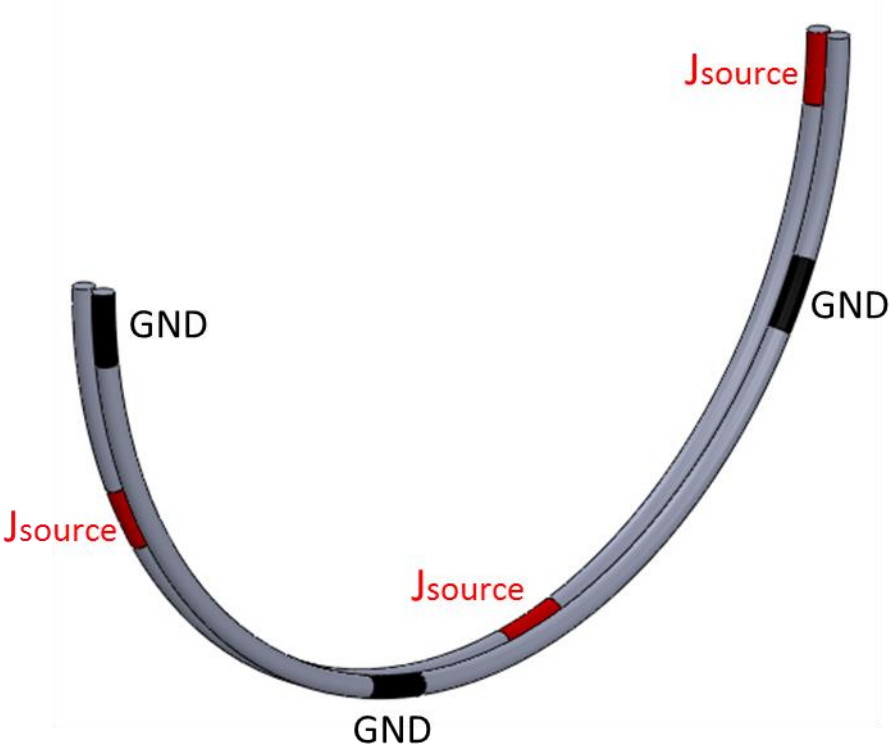

Figure 4-9 Illustration of constant density boundary condition on the Neurent basket electrode.

Constant normal current density simulation results

Figure 4-10 shows a comparison of normalized current densities for different electrode geometries. It also contains a 10% of the applied normalized current density contour (iso-current density contour) in each plot. In each simulation, the electrodes are supplied with same current density. The 10% iso-current density contour provides an indication of the region over which 90% of the injected current is distributed, thus providing an estimate of the ablation profile suitable for comparison among different electrode designs.

To assess the effects of electrode length on current density distribution, we compared a 0.75mm long to 5mm long electrode with same diameter. Our simulations indicate that current

density decreases faster with shorter electrode. For example, under electrode diameter of 1mm, the margin of 10% iso-current density contour is 0.5 mm with electrode length of 0.75 mm while the margin is over 5 mm with electrode length of 5 mm. Therefore, longer electrodes can create deeper and longer lesions.

For electrode diameter, we compared same long electrode with diameter of 0.1 mm to 1 mm. The results show that current density decreases faster with smaller electrode diameter. Under electrode length of 1mm, the margin of 10% iso-current density contour increases from 0.3 mm to 2.5 mm with diameter changes from 0.1 mm to 1 mm. Therefore, thicker electrode will create deeper lesion.

For short and thin electrode, the contour is six discontiguous oval zones around each electrode. For short but wider electrodes, the iso-current contours appear as three separated band-like zones. For longer but thin electrodes, the contours are contiguous along the electrode. The largest contour zone is created with longest and thickest electrode. Based on the recommendation from doctors, a separated and deep lesion is preferred in treating rhinitis. Therefore, a short but wide electrode is suggested and a longer space between two pairs of electrodes may be more likely to achieve desired ablation profiles in practice.

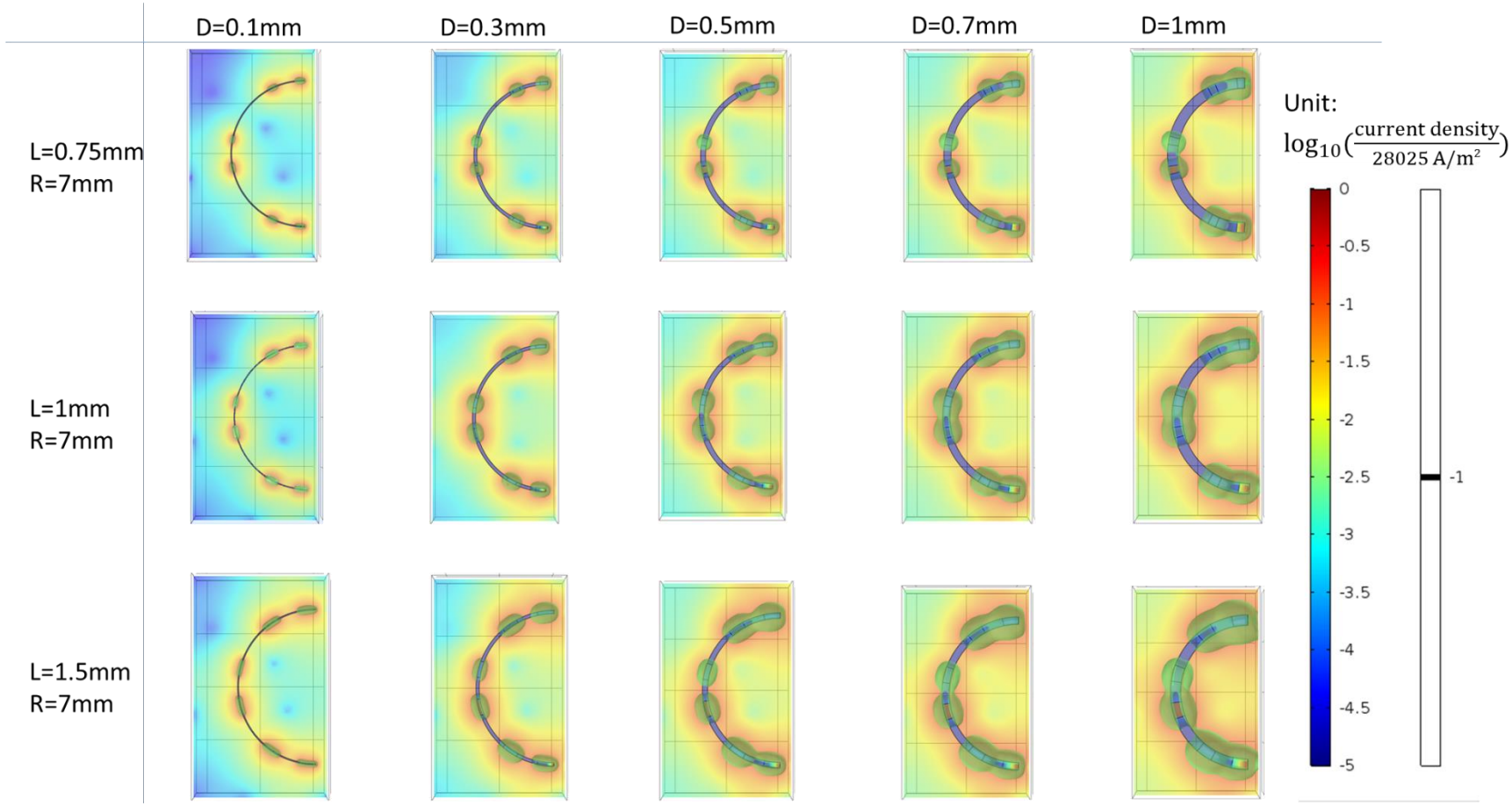
D=0.1mm
D=0.3mm
D=0.5mm
D=0.7mm
D=1mm
L=0.75mm
R=7mm
L=1mm
R=7mm
L=1.5mm
R=7mm
Unit:
$\log_{10}(\frac{\text{current density}}{28025\ \text{A/m}^2})$
0
-0.5
-1
-1.5
-2
-2.5
-3
-3.5
-4
-4.5
-5
-1

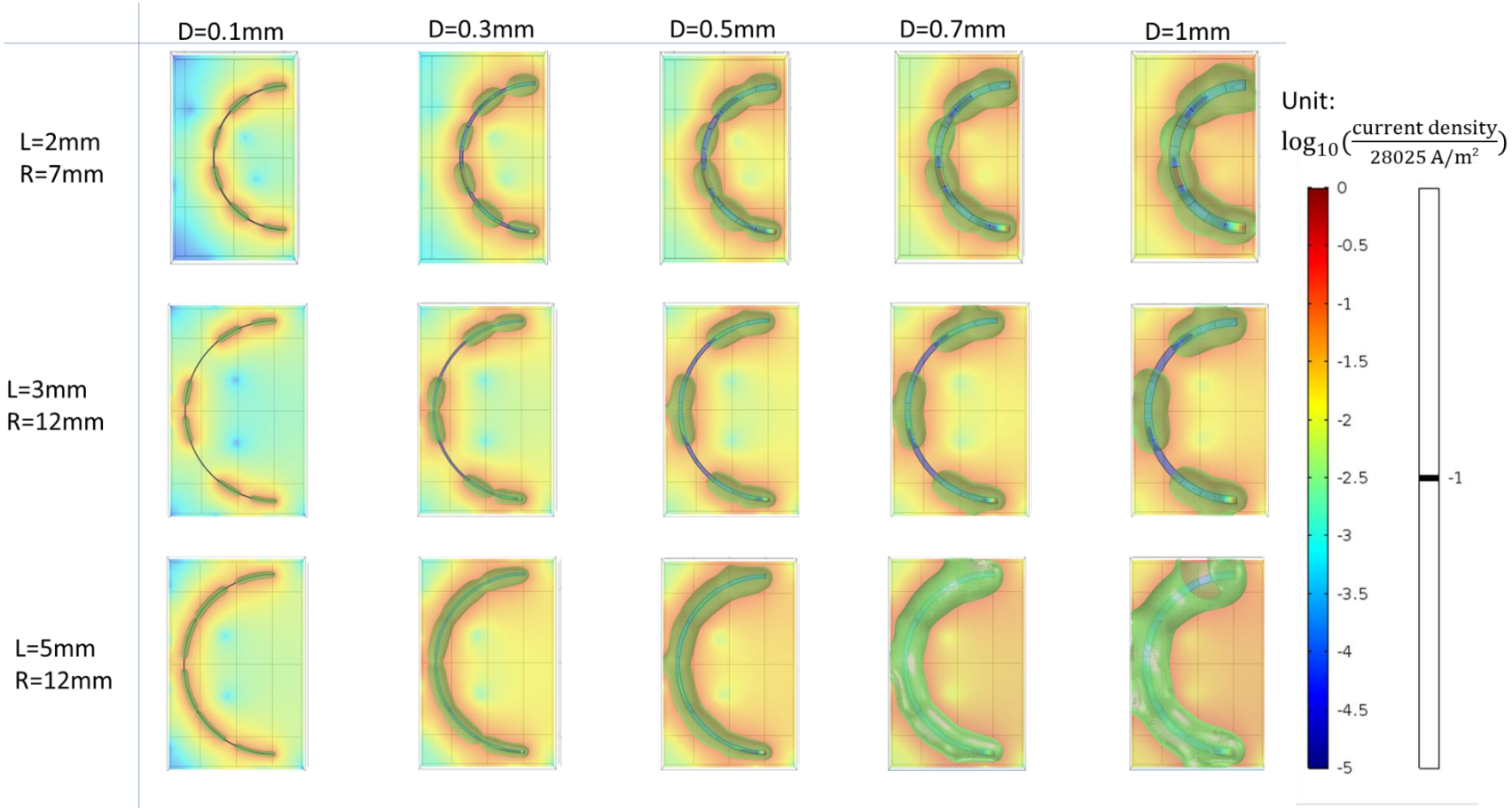
D=0.1mm
D=0.3mm
D=0.5mm
D=0.7mm
D=1mm
L=2mm
R=7mm
L=3mm
R=12mm
L=5mm
R=12mm
Unit:
$\log_{10}(\frac{\text{current density}}{28025\ \text{A/m}^2})$
0
-0.5
-1
-1.5
-2
-2.5
-3
-3.5
-4
-4.5
-5
-1

Figure 4-10 Current density distribution plot with 10% iso-current density contour for constant current density simulations with different electrode geometry.

Constant current simulation results

A constant current is applied on the electrode for varying geometries. With constant current, the current density changes as a function of electrode surface area. With longer and thicker electrode, the current density decreases. The total current maintains at 0.44A based on the number from egg white experiment. Figure 4-11 shows the normalized current density plot and 10% iso-current density plot. The 10% iso-current density plot here is the 10% contour plot of 28025 A/m^2 (applied in same current density simulations) instead of the actual applied current density to keep the contour comparable between simulations with changing current density. The contour become smaller and even invisible as the diameter and length of electrode become larger. Compared to the same-current density result, smaller current density will create smaller lesion. Therefore, the current needs to be adjusted higher with larger size electrode in the future experiments.

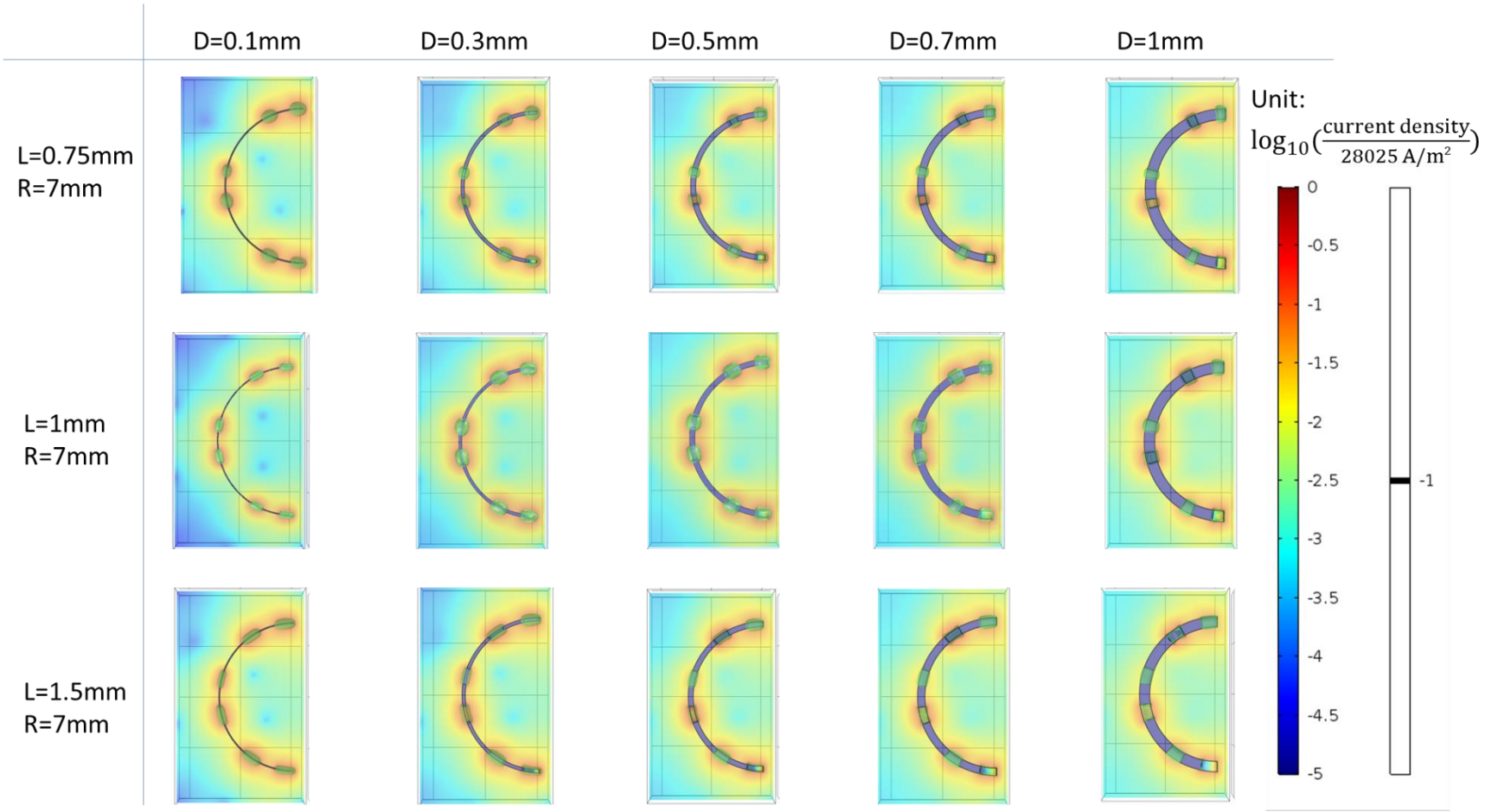
D=0.1mm
D=0.3mm
D=0.5mm
D=0.7mm
D=1mm
L=0.75mm
R=7mm
L=1mm
R=7mm
L=1.5mm
R=7mm
Unit:
$\log_{10}(\frac{\text{current density}}{28025\ \text{A/m}^2})$
0
-0.5
-1
-1.5
-2
-2.5
-3
-3.5
-4
-4.5
-5
-1

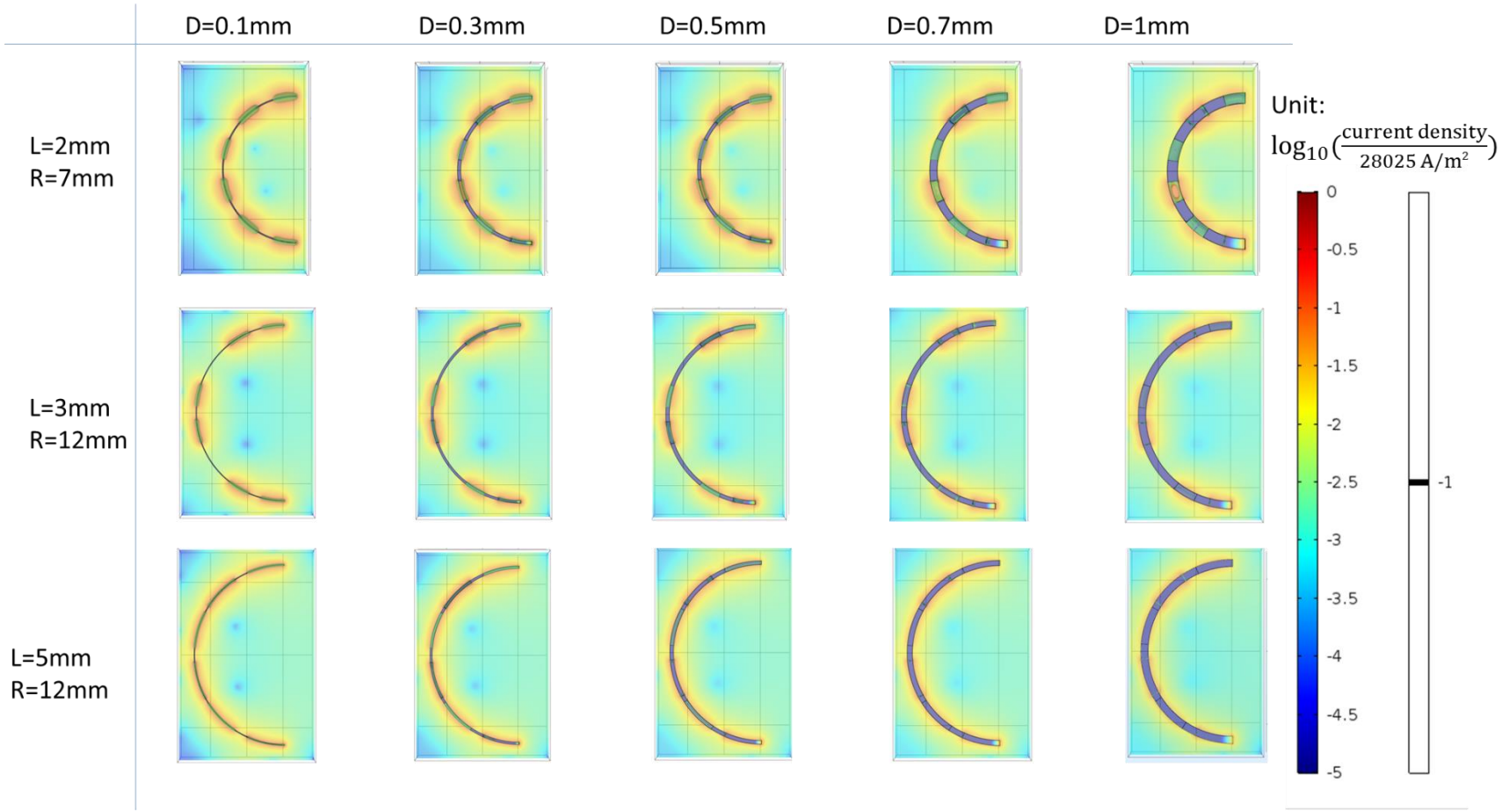
D=0.1mm
D=0.3mm
D=0.5mm
D=0.7mm
D=1mm
L=2mm
R=7mm
L=3mm
R=12mm
L=5mm
R=12mm
Unit:
$\log_{10}(\frac{\text{current density}}{28025\ \text{A/m}^2})$
0
-0.5
-1
-1.5
-2
-2.5
-3
-3.5
-4
-4.5
-5
-1

Figure 4-11 Current density distribution plot with 10% of iso-current density contour for constant current simulations with different electrode geometry.

Influence of duty cycle

Simulations

The voltage FEM analysis calculating electric fields and iso-therms is used to study the effects of duty cycle on ablation profiles. One simplified probe arch with electrode diameter of 0.3 mm and length of 1mm is placed into a rectangular liver tissue. The probe arch includes two parallel semicircle arc with distance of 0.05mm. There is one pair of electrodes on this probe arch due to computational limitation. The size of the liver tissue is $20\ mm \times 10\ mm \times 12\ mm$. The geometry is shown below.

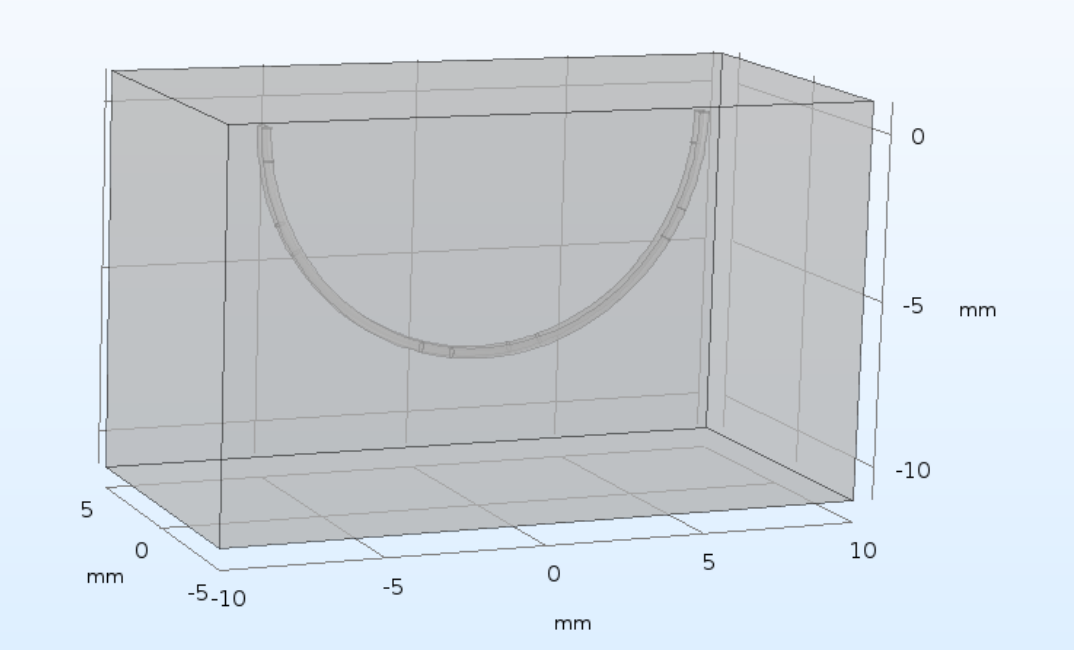

Figure 4-12 Simulation geometry for studying power duty cycle effects.

The initial temperature is 28 °C and thermal insulation is applied to the liver tissue outside. The active electrode provides 30 V as source voltage and the other ground electrode works as a return. The initial voltage is 0 V for the whole domain. The material properties are shown in Chapter 2. Voltage is applied on all the time, 50% and 20% of the time corresponding to simulations with duty cycle of 100%, 50% and 20%. One period is defined to be 20 s. The voltage power signal is shown in figure 4-13.

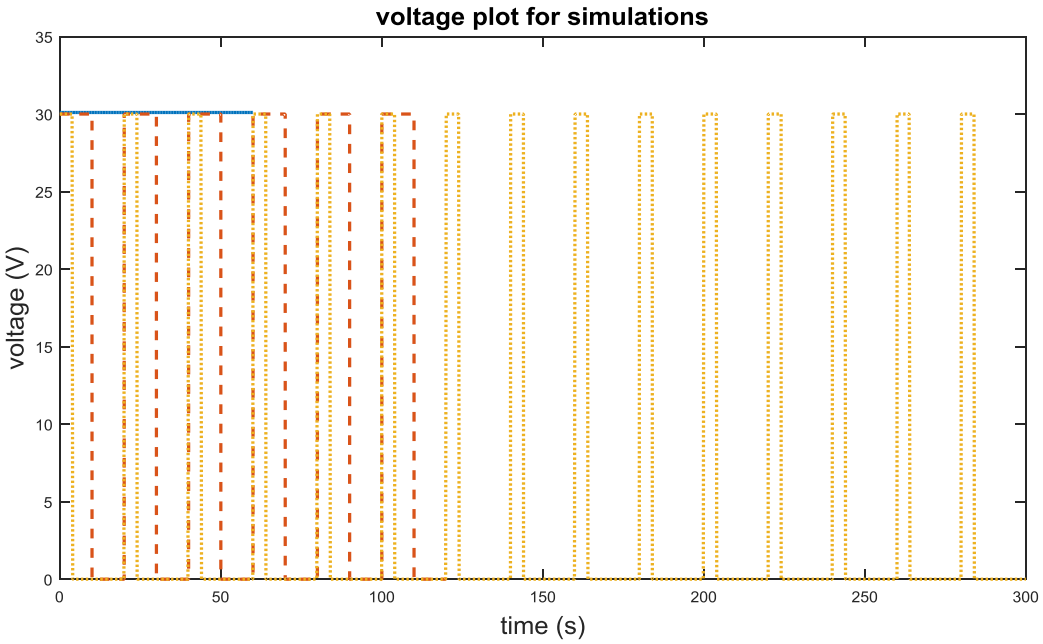

Figure 4-13 Voltage power plot for 100%, 50%, and 20% duty cycle simulations.

The mesh size is established in the same manner as the validation simulations in Chapter 3. The simulation time are 60s, 120s, and 300s with corresponding to 100%, 50%, and 20% duty cycle. The total ablation working time is the same for each simulation. The time step intervals is

0.5s. For the simulation, the impedance (R), power (P), temperature (T) and the integrated 50°C temperature contour are calculated. The simulations take 4, 18, 52 hours

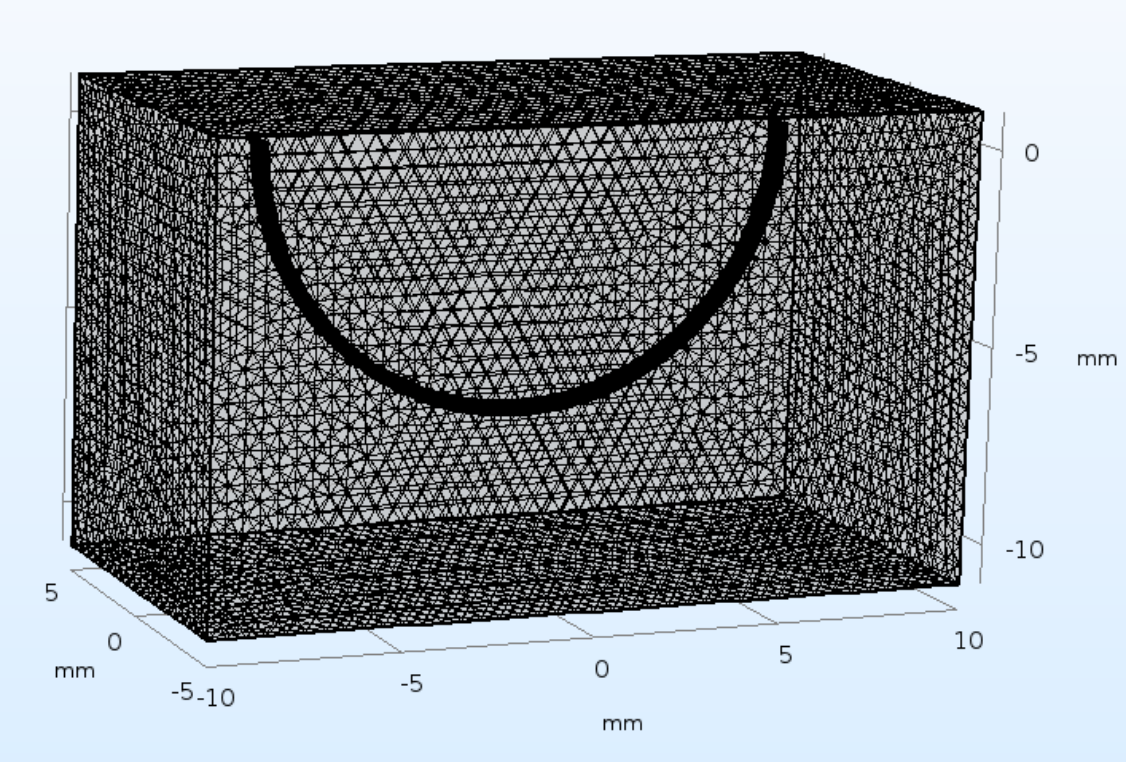

Figure 4-14 Mesh setup.

Results

Figure 4-15 shows a plot of tissue temperature with a probe point at a distance of 0.3mm from the center of active electrode with duty cycle of 100%, 50% and 20%. The data show that the temperature gradually increases with time. For each simulation, the highest temperature point are 82 °C at 60s, 69 °C at 110s, 44 °C at 284s corresponding to 100%, 50%, and 20% duty cycle. Figure 4-16 shows our temperature distribution plots and 50°C lesion contour in black line with variable applied duty cycle when highest temperature appears. Figure 4-17 shows the maximum lesion volume during the ablation procedure. The maximum lesion volume shows up at 60s (100%

duty cycle), 110s (50% duty cycle), and there is no lesion created for 20% duty cycle since the maximum temperature is 44°C during the whole procedure.

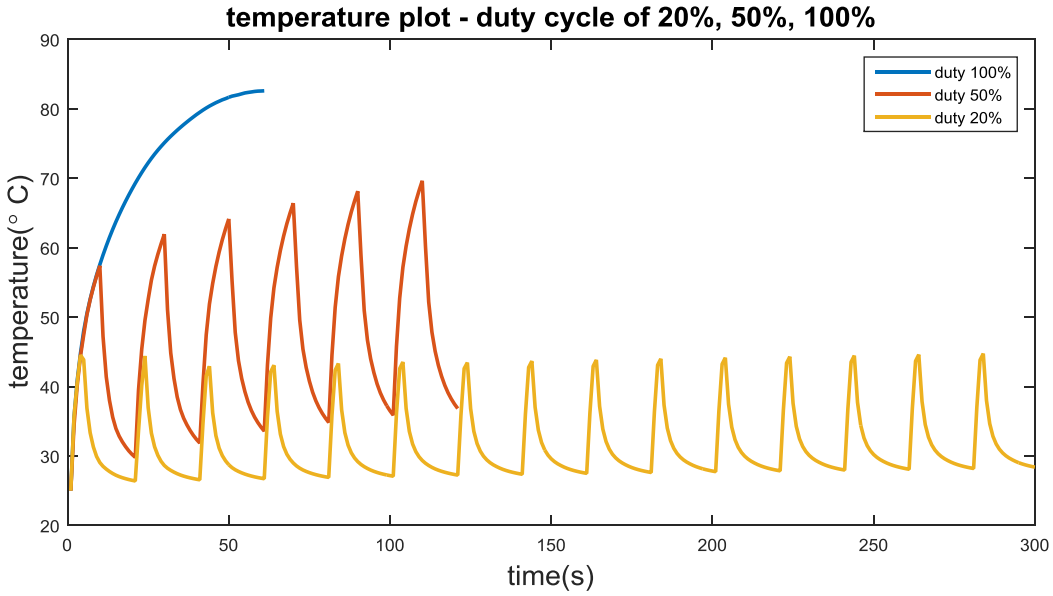

Figure 4-15 Tissue temperature plot for 100%, 50%, and 20% duty cycle.

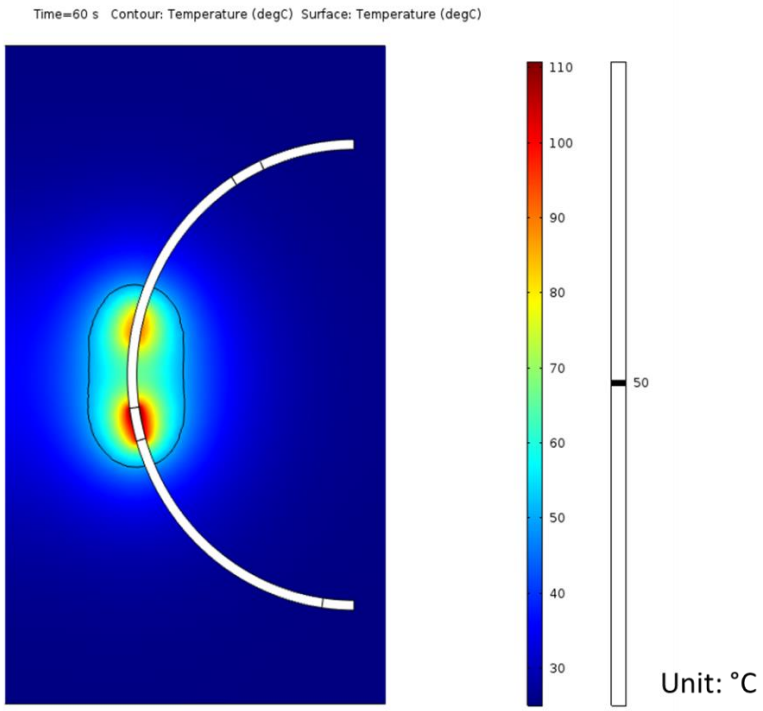

(a)

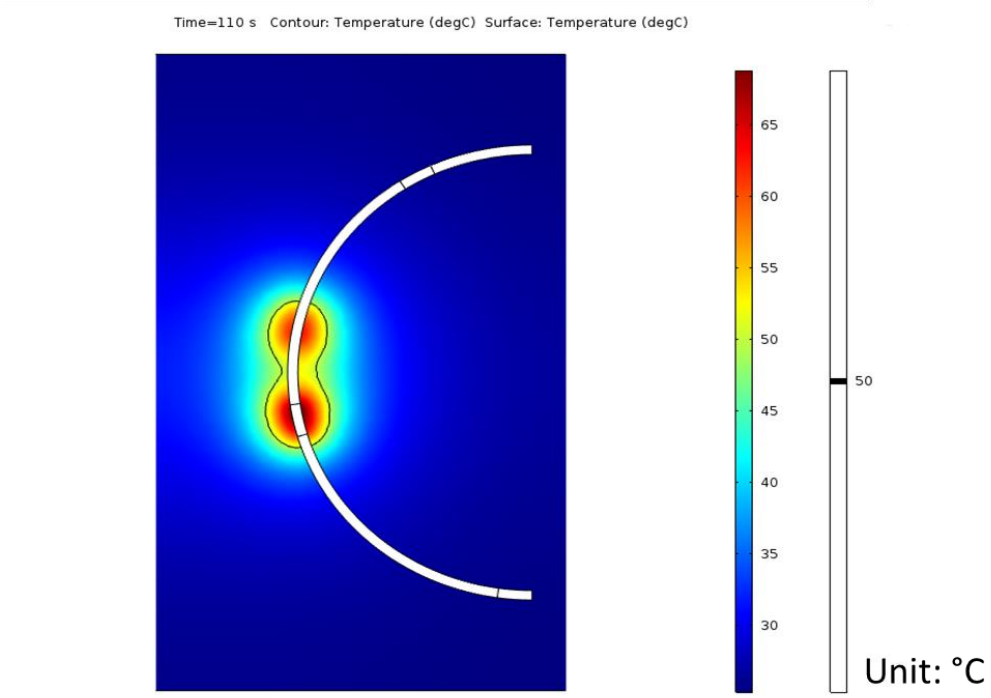
Time=110 s Contour: Temperature (degC) Surface: Temperature (degC)
65
60
55
50
45
40
35
30
50
Unit: °C

(b)

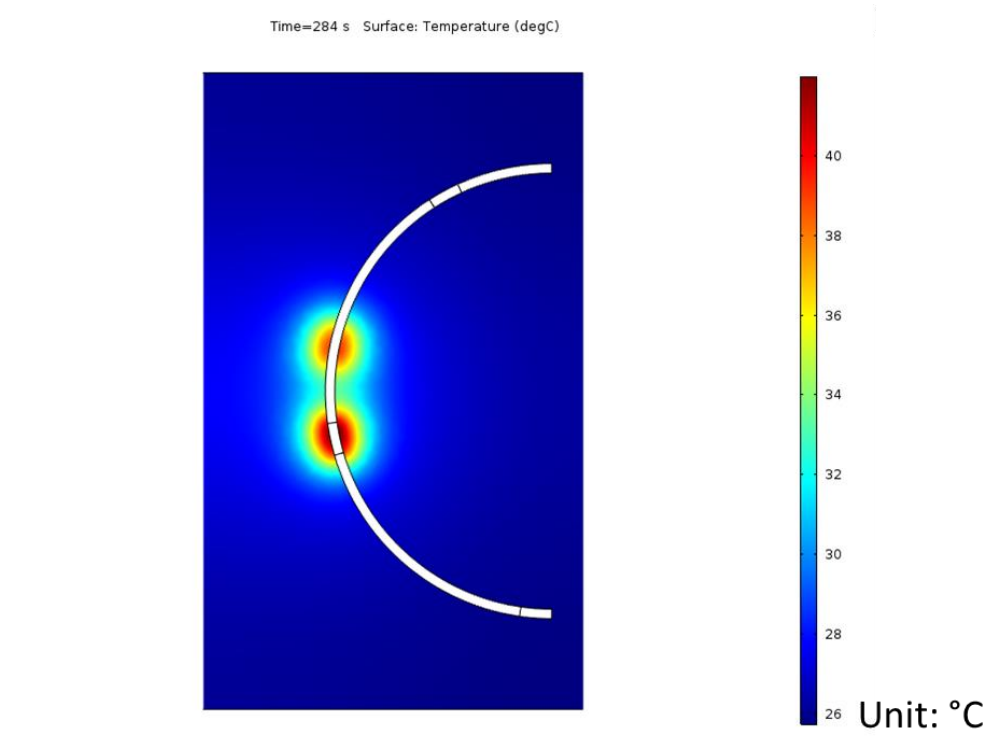
Time=284 s Surface: Temperature (degC)
40
38
36
34
32
30
28
26
Unit: °C

(c)

Figure 4-16 Surface temperature distribution plot with 50 °C contour at the highest temperature time.

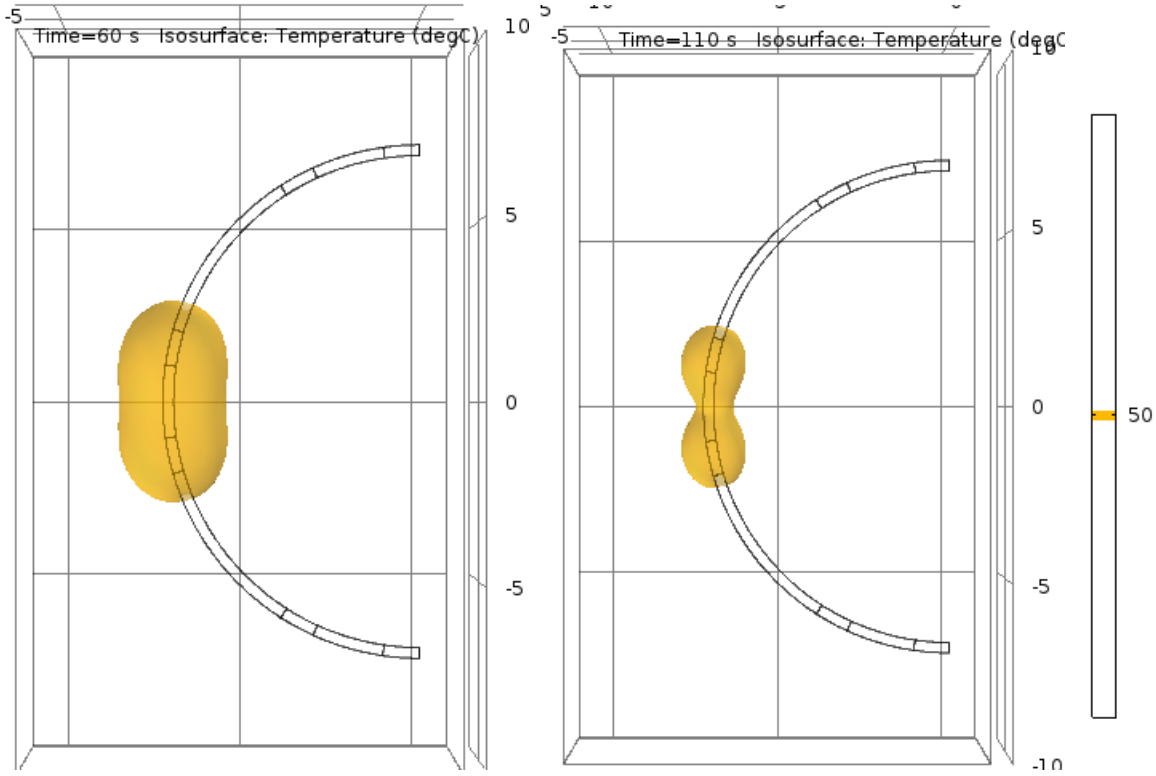

Figure 4-17 Maximum lesion contour for 100% and 50% duty cycle.

The largest lesion volume is created at the time with highest temperature of the ablation procedure. With higher duty cycle, the highest temperature and lesion volume increases. Lower duty cycle do not help with creating larger lesion under same ablation time. But lower lesion will increase tissue temperature gradually which may be safer in clinical practices. To create the same lesion with 100% duty cycle, a longer ablation working time is required with 50% duty cycle.

Chapter 5 - Conclusions and Future Work

Radiofrequency ablation is a new method proposed for treating rhinitis with a minimally invasive approach. Theoretical simulation models are a powerful tool to guide the device design and the selection of energy delivery strategies in treating rhinitis. We summarized the methodology for creating a computational model of the Neurent basket electrode. Comparison against experimental data showed a high correlation (R = 0.91) with simulations. Experimental thermal ablation zones created by the Neurent basket electrode in egg white were compared against simulation predictions. The thermal ablation zone from experiments were smaller than predicted lesion from simulation due to thermal convection in the egg white. FEM model results indicate the electrode diameter, length and duty cycle have large impact on the thermal lesion. A short but wider electrode with a maximum distance between pairs of electrodes is preferred to create desired separated (i.e. discontiguous) band-like zone of ablation around the electrodes. 50% duty cycle with longer ablation working time is recommended to create lesion with gradually increasing temperature and sufficient lesion volumes.

However, there are certain important limitations impeding the completion and accuracy of our model. One limitation is the lack of the experimental verification of the Neurent basket electrode with different electrode geometry. A comparison between *in vivo* experiments in the nasal cavity and simulations results using Neurent basket electrode would be of great value in the future work. It would also be valuable to investigate other parameters that will affect RF ablation treatment results, such as electrode phase shift.

Reference

[1] U. Martin, K. Bryden, M. Devoy, and P. Howarth, “Increased levels of exhaled nitric oxide during nasal and oral breathing in subjects with seasonal rhinitis,” *J. Allergy Clin. Immunol.*, vol. 97, no. 3, pp. 768–772, Mar. 1996.

[2] G. Loureiro, B. Tavares, D. Machado, and C. Pereira, “Nasal provocation test in the diagnosis of allergic rhinitis,” in *Allergic rhinitis*, InTech, 2012.

[3] D. K. Sur and S. Scandale, “Treatment of allergic rhinitis,” *Am. Fam. Physician*, vol. 81, no. 12, p. 1440, 2010.

[4] A. Rhinitis and A. Khuntia, “Allergic Rhinitis,” *J Allergy Clin Immunol*, vol. 108, pp. S147–334, 2001.

[5] “Improvement of symptoms of non-allergic chronic rhinitis by local treatment with capsaicin - LACROIX - 1991 - Clinical & Experimental Allergy - Wiley Online Library.” [Online]. Available: https://onlinelibrary.wiley.com/doi/abs/10.1111/j.1365-2222.1991.tb00852.x. [Accessed: 09-Aug-2018].

[6] K. Aoishi *et al.*, “Treatment of allergic rhinitis with intranasal infusion of botulinum toxin type A in mice,” *Life Sci.*, vol. 147, pp. 132–136, 2016.

[7] I.-R. T. P. LTD (https://www.informit.org/researchers/who-is-informit), “Put the heat on non-allergic rhinitis,” *AJP Aust. J. Pharm.*, vol. 92, no. 1098, p. 42, Nov. 2011.

[8] R. A. Settipane and D. R. Charnock, “Epidemiology of rhinitis: allergic and nonallergic.,” *Clin. Allergy Immunol.*, vol. 19, pp. 23–34, 2007.

[9] P. P. Caffier, H. Scherer, K. Neumann, S. Lück, H. Enzmann, and A. Haisch, “Diode laser treatment in therapy-resistant allergic rhinitis: impact on nasal obstruction and associated symptoms,” *Lasers Med. Sci.*, vol. 26, no. 1, pp. 57–67, Jan. 2011.

[10] F. Braido, F. Arcadipane, F. Marugo, M. Hayashi, and R. Pawankar, “Allergic rhinitis: current options and future perspectives,” *Curr. Opin. Allergy Clin. Immunol.*, vol. 14, no. 2, pp. 168–176, 2014.

[11] J. Bousquet *et al.*, “Allergic Rhinitis and its Impact on Asthma (ARIA) 2008*,” *Allergy*, vol. 63, pp. 8–160, Apr. 2008.

[12] E. J. Berjano, “Theoretical modeling for radiofrequency ablation: state-of-the-art and challenges for the future,” *Biomed. Eng. Online*, vol. 5, no. 1, p. 24, 2006.

[13] C. N. Shealy, “Percutaneous radiofrequency denervation of spinal facets,” *J. Neurosurg.*, vol. 43, no. 4, pp. 448–451, Oct. 1975.

[14] M. A. D’Arsonval, “Physiological effect of alternative currents,” *CR Soc Biol*, vol. 43, pp. 283–286, 1891.

[15] H. Cushing, “Electrosurgery as an aid to the removal of intracranial tumors,” *Surg Gynecol Obstet*, vol. 47, pp. 751–784, 1928.

[16] W. T. Bovie, “Electrosurgical apparatus,” US1813902A, 14-Jul-1931.

[17] J. P. Mcgahan, P. D. Browning, J. M. Brock, and H. Tesluk, “Hepatic ablation using radiofrequency electrocautery.,” *Invest. Radiol.*, vol. 25, no. 3, pp. 267–270, 1990.

[18] S. N. Goldberg, G. S. Gazelle, S. L. Dawson, W. J. Rittman, P. R. Mueller, and D. I. Rosenthal, “Tissue ablation with radiofrequency: effect of probe size, gauge, duration, and temperature on lesion volume,” *Acad. Radiol.*, vol. 2, no. 5, pp. 399–404, 1995.

[19] J. P. McGahan, P. Schneider, J. M. Brock, and H. Tesluk, “Treatment of liver tumors by percutaneous radiofrequency electrocautery,” *Semin. Interv. Radiol.*, vol. 10, no. 2, pp. 143–149, 1993.
[20] R. F. LeVeen, “Laser hyperthermia and radiofrequency ablation of hepatic lesions,” *Semin. Interv. Radiol.*, vol. 14, pp. 313–324, Sep. 1997.
[21] S. Nahum Goldberg, G. Scott Gazelle, L. Solbiati, W. J. Rittman, and P. R. Mueller, “Radiofrequency tissue ablation: Increased lesion diameter with a perfusion electrode,” *Acad. Radiol.*, vol. 3, no. 8, pp. 636–644, Aug. 1996.
[22] M. L. Hytönen, L. J. J. Bäck, A. V. Malmivaara, and R. P. Roine, “Radiofrequency thermal ablation for patients with nasal symptoms: a systematic review of effectiveness and complications,” *Eur. Arch. Otorhinolaryngol.*, vol. 266, no. 8, pp. 1257–1266, Aug. 2009.
[23] E. J. Kezirian, N. B. Powell, R. W. Riley, and J. E. Hester, “Incidence of Complications in Radiofrequency Treatment of the Upper Airway,” *The Laryngoscope*, vol. 115, no. 7, pp. 1298–1304, Jul. 2005.
[24] S. Celiker, A. Rosenblad, and B. Wilhelmsson, “A radiofrequency vs topical steroid treatment of chronic nasal obstruction: A prospective randomized study of 84 cases,” *Acta Otolaryngol. (Stockh.)*, vol. 131, no. 1, pp. 79–83, Jan. 2011.
[25] D. Haemmerich, “Biophysics of Radiofrequency Ablation,” *Crit. Rev. Biomed. Eng.*, vol. 38, no. 1, 2010.
[26] H. TSENG, S.-E. LIN, Y.-L. CHANG, M.-H. CHEN, and S.-H. HUNG, “Determining the critical effective temperature and heat dispersal pattern in monopolar radiofrequency ablation using temperature-time integration,” *Exp. Ther. Med.*, vol. 11, no. 3, pp. 763–768, Mar. 2016.
[27] I. A. Chang, “Considerations for Thermal Injury Analysis for RF Ablation Devices,” *Open Biomed. Eng. J.*, vol. 4, pp. 3–12, Feb. 2010.
[28] P. Pezeshki, “Bone Targeted Radiofrequency Ablation (RFA) Electrodes for the Treatment of Appendicular and Vertebral Metastases,” Ph.D., University of Toronto (Canada), Canada, 2014.
[29] X. Li *et al.*, “Comparison of microwave ablation and multipolar radiofrequency ablation, both using a pair of internally cooled interstitial applicators: Results in ex vivo porcine livers,” *Int. J. Hyperthermia*, vol. 27, no. 3, pp. 240–248, May 2011.
[30] “Detailed Explanation of the Finite Element Method (FEM).” [Online]. Available: https://www.comsol.com/multiphysics/finite-element-method. [Accessed: 10-Apr-2018].
[31] “Finite element method,” *Wikipedia*. 08-Apr-2018.
[32] A. V. Shahidi and P. Savard, “A finite element model for radiofrequency ablation of the myocardium,” *IEEE Trans. Biomed. Eng.*, vol. 41, no. 10, pp. 963–968, Oct. 1994.
[33] P. Li, S. J. Eckels, N. Zhang, and G. W. Mann, “Effects of Parallel Processing on Large Eddy Simulations in ANSYS Fluent,” p. V01BT26A004, Jul. 2016.
[34] H. H. Pennes, “Analysis of tissue and arterial blood temperatures in the resting human forearm. 1948,” *J. Appl. Physiol. Bethesda Md 1985*, vol. 85, no. 1, pp. 5–34, Jul. 1998.
[35] Z. Wang, H. Luo, S. Coleman, and A. Cuschieri, “Bicomponent Conformal Electrode for Radiofrequency Sequential Ablation and Circumferential Separation of Large Tumors in Solid Organs: Development and In Vitro Evaluation,” *IEEE Trans. Biomed. Eng.*, vol. 64, no. 3, pp. 699–705, Mar. 2017.

[36] M. J. Borrelli, L. L. Thompson, C. A. Cain, and W. C. Dewey, “Time-temperature analysis of cell killing of BHK cells heated at temperatures in the range of 43.5 degrees C to 57.0 degrees C,” *Int. J. Radiat. Oncol. Biol. Phys.*, vol. 19, no. 2, pp. 389–399, Aug. 1990.
[37] “Boundary value problem,” *Wikipedia*. 02-Feb-2018.
[38] “How to Make Boundary Conditions Conditional in Your Simulation,” *COMSOL Multiphysics©*. .
[39] D. Haemmerich, L. Chachati, A. S. Wright, D. M. Mahvi, F. T. Lee, and J. G. Webster, “Hepatic radiofrequency ablation with internally cooled probes: effect of coolant temperature on lesion size,” *IEEE Trans. Biomed. Eng.*, vol. 50, no. 4, pp. 493–500, Apr. 2003.
[40] D. J. Schutt and D. Haemmerich, “Effects of variation in perfusion rates and of perfusion models in computational models of radio frequency tumor ablation,” *Med. Phys.*, vol. 35, no. 8, pp. 3462–3470.
[41] G. Shafirstein *et al.*, “Conductive interstitial thermal therapy device for surgical margin ablation: In vivo verification of a theoretical model,” *Int. J. Hyperthermia*, vol. 23, no. 6, pp. 477–492, Jan. 2007.
[42] P. Prakash, C. Ganta, W. Beard, J. Lillch, Y. Song, and D. Townley, “Pre-clinical assessment of radiofrequency ablation for nasal tissue ablation in an in-vivo porcine model.”
[43] L. Lobik, R. J. Leveillee, and M. F. Hoey, “Geometry and Temperature Distribution during Radiofrequency Tissue Ablation: An Experimental ex Vivo Model,” *J. Endourol.*, vol. 19, no. 2, pp. 242–247, Mar. 2005.
[44] G. W. Divkovic, M. Liebler, K. Braun, T. Dreyer, P. E. Huber, and J. W. Jenne, “Thermal Properties and Changes of Acoustic Parameters in an Egg White Phantom During Heating and Coagulation by High Intensity Focused Ultrasound,” *Ultrasound Med. Biol.*, vol. 33, no. 6, pp. 981–986, Jun. 2007.
[45] J. Wren, O. Eriksson, K. W\a ardell, and D. Loyd, “Analysis of temperature measurement for monitoring radio-frequency brain lesioning,” *Med. Biol. Eng. Comput.*, vol. 39, no. 2, pp. 255–262, 2001.
[46] E. R. Cosman Jr, J. R. Dolensky, and R. A. Hoffman, “Factors that affect radiofrequency heat lesion size,” *Pain Med.*, vol. 15, no. 12, pp. 2020–2036, 2014.

Appendix A - *In Vivo* Radiofrequency Ablation Experiments for Nasal Tissue

The experiments described in this appendix is based on the report: Preclinical assessment of radiofrequency ablation for nasal tissue ablation in an *in vivo* porcine model, written by Punit Prakash, Yuqi Song, Chandra Ganta, Jim Lillch, Warren Beard, and Dave Townley [42].

The objective of the experiments was to characterize damage induced in nasal mucosa and submucosal structures after RF ablation with Neurent basket electrode probe. This study is specific to investigate the deterministic identification and evaluation of changes to the functional characteristics of autonomic and vascular supply to nasal mucosal tissue after 48 hours following the application of RF ablation procedure.

The probe used in this experiment is described in Chapter 4 – Nuerent basket electrode, and the RF generator mentioned in Chapter 3 is used to deliver radiofrequency energy. The experiments were performed on 40 – 50 kg female domestic swine (s) under the approval of the KSU Institutional Animal Care and Use Committee (IACUC) Protocol No. 3853.

A customized applicator connector was selected and connected the probe with RF generator. During the experiment, the surgeon placed the probe into pig nostril with a distance indicator on the device such that 9 cm marking was at the entrance to the nostril. The indicator is shown in figure A-1. After ablation, the device was rotated 180° and the ablation procedure was performed. The device was then retracted back to the 6cm position for ablation, then rotated 180° and ablation repeated. The probe was retracted back again to the 3 cm position for ablation, then rotated 180° and performed ablation again. The whole procedure is repeated for the other nostril. There are a total of 2 treatments on one position, 6 treatments on 3 sites per cavity, and a total of 12 treatments per animal.

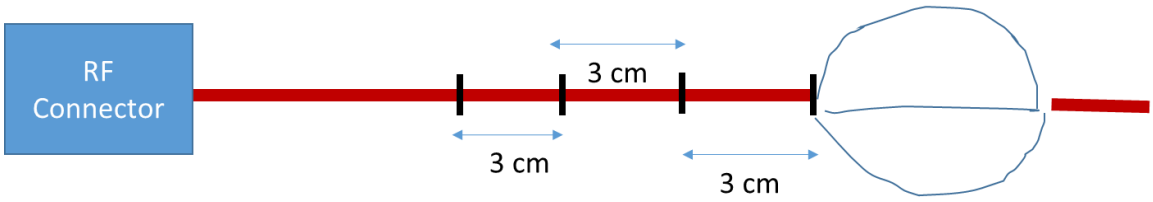

Figure A-1 Electrode position with pig nares during *in vivo* ablation study.

A total number of three experiments were performed in this research including two non-survival studies and one 48 hour survival study. In the non-survival study, the animals were euthanized after completion of ablations. In survival study, the animals were survived to 48 hours before euthanizing. Following euthanasia, tissue samples were harvested for histopathologic analysis.

Figure A-2 is the nasal cavity dissection image. Figure A-3 is the tissue microscopic examination image. Tissue were fixed in 10% buffered neutral formalin and routinely processed, embedded in paraffin, sectioned at 5 μm, and stained with H&E before the examination. The microscopic images were then interpreted by a board-certified pathologist (C.G).

Figure A-2 Nasal cavity dissection

A

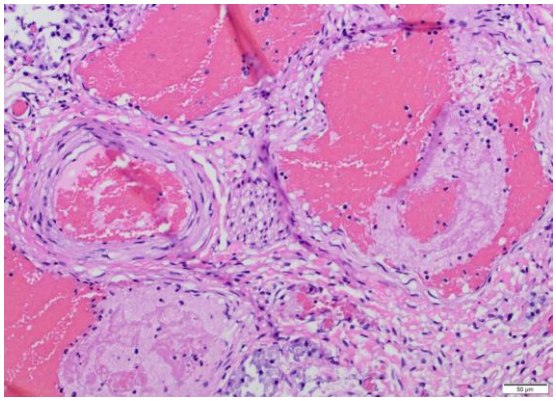

B

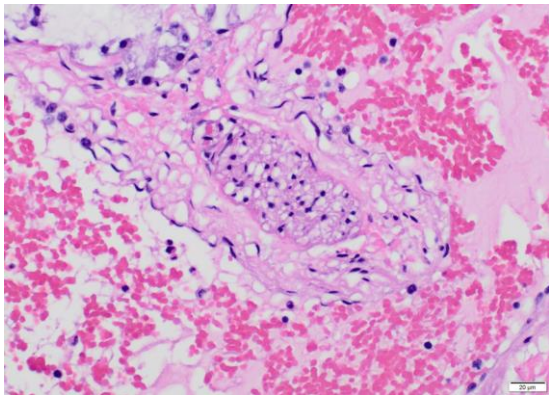

Figure A-3 Microscopic examination